Materials Today Bio 35 (2025) 102445

Contents lists available at ScienceDirect

Materials Today Bio

journal homepage: www.journals.elsevier.com/materials-today-bio

Empowering chemotherapy-induced antitumor immunity by multi-targeted synergistic combination nanomedicine for triple-negative breast cancer

Ibrahim Alradwan[a,b], Pei Zhi[a], Abdulmottaleb E. Zetrini[a,c], Liting Wang[a], Chunsheng He[a], Mahya Rezaeifarimani[a], Jeffrey T. Henderson[a], Andrew M. Rauth[d], Xiao Yu Wu[a,*]

[a] *Advanced Pharmaceutics and Drug Delivery Laboratory, Leslie Dan Faculty of Pharmacy, University of Toronto, 144 College Street, Toronto, Ontario, Canada, M5S 3M2*
[b] *Advanced Diagnostics and Therapeutics Institute, King Abdulaziz City for Science and Technology (KACST), Riyadh, 11461, Saudi Arabia*
[c] *Department of Pharmaceutics, Faculty of Pharmacy, University of Tripoli, Tripoli, Libya*
[d] *Departments of Medical Biophysics and Radiation Oncology, University of Toronto, 610 University Ave, Toronto, Ontario, Canada, M5G 2M9*

ARTICLE INFO

Keywords:
Triple-negative breast cancer (TNBC)
Synergistic drug combination
Polymer lipid hybrid nanoparticles (PLN)
Integrin targeting
Immunogenic cell death (ICD)
Boosting immune response
Inhibiting metastasis

ABSTRACT

Triple negative breast cancer (TNBC) is an aggressive malignancy characterized by early recurrence, high metastatic burden, and resistance to conventional therapies, largely due to the absence of targetable receptors and an immunosuppressive tumor microenvironment. To address these limitations, our lab has engineered a multifunctional nanotherapeutic system iRGD-DOX-oHA-PLN comprising polymer-lipid nanoparticles co-loaded with doxorubicin (DOX) and oligomeric hyaluronic acid (oHA) and functionalized with the tumor-penetrating integrin-targeting iRGD peptide. This rationally designed platform capitalizes on the sequential targeting mechanism: integrin-mediated tumor penetration and endocytosis via iRGD, followed by CD44 engagement through oHA to enhance intracellular drug delivery and suppresses cell motility. iRGD-DOX-oHA-PLN significantly improved cellular uptake, intratumoral accumulation, and cytotoxic efficacy in TNBC cells and tumors. Notably, it enhanced immunogenic cell death, characterized by increased calreticulin exposure, ATP and HMGB1 levels, triggering potent anti-tumor immune responses. Intravenous treatment led to elevated $CD8^+$ T-cell infiltration, granzyme B expression, and secretion of pro-inflammatory cytokines (TNF-α, IFN-γ), while concurrently suppressing immunosuppressive mediators including IL-6, regulatory T cells, and tumor-associated macrophages. Over a four-week treatment period, iRGD-DOX-oHA-PLN effectively inhibited primary tumor growth and systemic pulmonary metastases in a syngeneic orthotopic TNBC mouse model. These findings demonstrate the therapeutic potential of simultaneously targeting integrin-CD44 signaling and the immunosuppressive niche using a dual-functional nanomedicine to overcome drug resistance and immune evasion in TNBC, offering a promising strategy for metastatic cancer intervention.

1. Introduction

Breast cancer remains the most diagnosed cancer and a leading cause of cancer-related death among women worldwide. Among its subtypes, triple-negative breast cancer (TNBC) represents the most aggressive and lethal form, characterized by the absence of estrogen receptor, progesterone receptor, and HER2 expression. TNBC patients face nearly a threefold higher risk of recurrence within five years compared to other breast cancer subtypes, with limited treatment options and poor long-term survival outcomes [1]. Recent advancements in immunotherapy, particularly immune checkpoint inhibitors, have modestly improved outcomes in TNBC. For example, pembrolizumab, a PD-1 inhibitor, has demonstrated clinical benefits in high-risk, early-stage TNBC with high PD-L1 expression [2,3]. However, only a subset of patients develops durable responses, and resistance remains a major obstacle [4].

A primary obstacle in treating solid tumors like TNBC is its complex and immunosuppressive tumor microenvironment (TME), which promotes tumor progression and metastasis by recruiting regulatory immune cells such as regulatory T cells (Tregs), myeloid-derived suppressor cells (MDSCs), and M2-polarized macrophages-and by fostering the production of anti-inflammatory cytokines like IL-10 and TGF-β within the tumor stroma that contribute the immune cells

---

* Corresponding author.
E-mail address: sxy.wu@utoronto.ca (X.Y. Wu).

https://doi.org/10.1016/j.mtbio.2025.102445
Received 24 July 2025; Received in revised form 3 October 2025; Accepted 19 October 2025

exhaustion [5,6]. These factors greatly diminish the effectiveness of treatments, including chemotherapy, radiotherapy, or immunotherapy [6,7].

One of the key TME components is hyaluronic acid (HA), a glycosaminoglycan abundantly present in the extracellular matrix of solid tumors. The physical abundance of high-molecular weight HA surrounding the tumors has been shown to facilitate immune evasion by shielding tumor cells from immune cells and promoting the differentiation of immunosuppressive cells through CD44 interactions of immune cells with the proximity of HA for cancer cells survival, proliferation, and adaptations of the metastasis/migration pathways [8–10].

In contrast, oligomeric hyaluronic acid (oHA), a low molecular weight ≤10 kDa, has been shown to disrupt the CD44 clustering and mitigates oncogenic and pro-tumorigenic signaling of cancer cells [8]. Moreover, oHA has been shown to exhibit distinct immunomodulatory effects [11–14]. Acting as a damage-associated molecular pattern (DAMP), oHA can reprogram the immune milieu by enhancing macrophages polarization to M1, promote dendritic cell maturation, increase interferon-γ (IFN-γ) release, and facilitate CD8$^+$ T-cell tumor infiltration [11,12,15]. Consequently, oHA holds a promise as a therapeutic agent, potentially boosting anti-tumor immunity and enhancing the overall efficacy of combination treatments.

As a first-line treatment for TNBC, the anthracycline chemotherapeutic doxorubicin (DOX) is established to induce immunogenic cell death (ICD), characterized by calreticulin (CRT) exposure on the cell surface and the release of ATP and HMGB1, which collectively promote antigen-presenting cell activation and stimulate cytotoxic T-cell mediated immune responses [16,17]. Along with cytotoxic T-cell activation, the natural killer (NK) cells and CD4$^+$ T cells can also produce granzyme B (GrB) and IFN-γ leading to the destruction of cancer cells [18,19]. However, the clinical utility of DOX is hampered by multidrug resistance, off-target and systemic toxicity (including cardiotoxicity and myelosuppression), and the hostile hypoxic and acidic immunosuppressive tumor microenvironment [20–22].

Controlled-release nanoformulations with synergistic drug combinations present a potent solution to overcome these challenges and enhance treatment efficacy [23–25]. Specifically, our developed formulation combines internalizing RGD (iRGD)-functionalized nanoparticles with DOX and oHA loaded into polymer lipid hybrid nanoparticles (iRGD-DOX-oHA-PLN). The iRGD peptide selectively targets αvβ3 and αvβ5 integrins as well as neuropilin-1 (NRP-1), which are abundantly expressed in TNBC tumor vasculature and cells, thereby improving targeted drug delivery to the tumor site [26,27]. Our previous studies have demonstrated significant anti-tumor and anti-metastatic effects using this formulation in orthotopic xenografts of MDA-MB-231 and MDA-MB-436 (BRCA1/2 mutant) TNBC tumors [14,28]. Additionally, oHA was found to decrease chemoresistance to DOX by inhibiting DNA damage repair proteins and reducing the expression of drug efflux pumps [14,28]. In this study, we hypothesize that the iRGD-DOX-oHA-PLN formulation not only enhances tumor-targeted delivery and synergizes chemotherapy via the iRGD-integrin and CD44-mediated pathways, but also actively remodels the TME to potentiate antitumor immunity. To validate this, we employ a spontaneously metastasizing, immunocompetent syngeneic TNBC mouse model, which recapitulates both the aggressive metastatic behavior and immune contexture of human TNBC. By leveraging this clinically relevant model, our study aims to confirm and mechanistically extend previous findings, demonstrating that multifunctional nanotherapeutics can orchestrate a coordinated attack on TNBC through vascular targeting, TME modulation, and immune reprogramming.

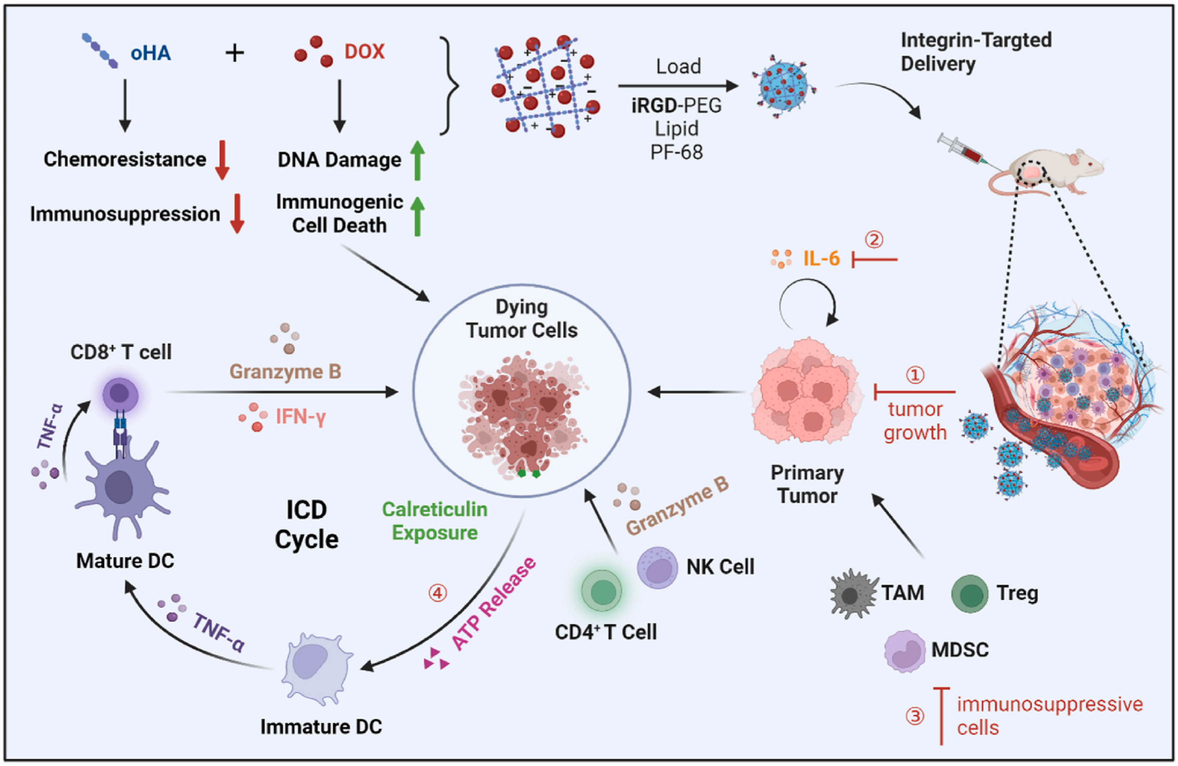

Fig. 1. Schematic illustration of the developed iRGD-DOX-oHA-PLN formulation and the proposed mechanism through which the synergistic effects of DOX and oHA modulate the immunosuppressive TME and enhance DOX cytotoxicity for TNBC treatment. The iRGD-DOX-oHA-PLN was synthesized through a one-pot self-assembly method. These nanoparticles were intravenously administered to mice bearing orthotopic TNBC tumors. The iRGD-DOX-oHA-PLN demonstrated potent anti-tumor and anti-metastatic effects through multiple mechanisms: 1) targeted accumulation in the tumor, leading to induced apoptosis of tumor cells; 2) inhibition of IL-6 production by oHA, which is a crucial factor in tumor growth and immunosuppression; 3) modulation and reduction of immunosuppressive cells; 4) induction of ICD, culminating in the recruitment and activation of cytotoxic CD8$^+$ T cells. NK cell: natural killer cell. Treg: T regulatory cell. MDSC: myeloid-derived suppressor cell.

As illustrated in Fig. 1, the iRGD-functionalization is expected to enhance the accumulation of nanoparticles within the primary tumor, increasing drug accumulation. The combination of DOX and oHA in an iRGD-conjugated nanocarrier is designed to modify the immunosuppressive TME by reducing interleukin-6 (IL-6) levels, diminishing immunosuppressive cell populations, and more effectively initiating ICD. Overall, our iRGD-DOX-oHA-PLN formulation offers a potent and comprehensive therapeutic strategy that combines cytotoxic and immunomodulatory actions to combat TNBC metastasis effectively.

2. Experimental section

Chemicals: Doxorubicin hydrochloride (Cat# HY-15142 A; ≥98 % purity) was purchased from MedChemExpress LLC (Monmouth Junction, New Jersey, USA). Polyoxyethylene (100) stearate (Myrj59) (Cat# P3690; purity ≥98 %) and Polyoxyethylene (40) stearate (Myrj52) (Cat# P3440) were obtained from Sigma-Aldrich (Oakville, ON, Canada). N-(3-Dimethylaminopropyl)-N′-ethylcarbodiimide hydrochloride (EDC) (Cat# 03450; purity ≥98 %) and N-hydroxysuccinimide (NHS) (Cat# 130672; purity ≥97 %) were also sourced from Sigma-Aldrich. Unless otherwise specified, all other chemicals were analytical grade and procured from Sigma-Aldrich.

The oligomeric hyaluronic acid (oHA, <10 kDa, pharmaceutical/cosmetic-grade, as per manufacturer) was purchased from Bloomage Biotech Co., Ltd. (Shandong, China). The cyclic peptide iRGD [c (CRGDRGPDC)] (purity >96 %) was obtained from LifeTein (Somerset, NJ, USA) (Cat# LT216216). D-Luciferin potassium salt (Cat# 14681; purity ≥98 %) was purchased from Cayman Chemical (Ann Arbor, MI, USA).

Cell culture: The 4T1-luc cell line was purchased from Caliper Life Sciences (Hopkinton, MA, USA). The RAW 264.7 cell line (ATCC TIB-71) was purchased from the American Type Culture Collection (ATCC) (Manassas, VA, USA). Cell lines were confirmed to be pathogen-free by the supplier using IMPACT Profile I. Mouse 4T1-luc TNBC cells were grown in RPMI-1640 medium (Gibco, Boston, MA, USA) containing 2 mM L-glutamine, 10 mM HEPES, 1 mM sodium pyruvate, 4.5 g L^{-1} glucose, 1.5 g L^{-1} sodium bicarbonate, and fetal bovine serum (FBS) to a final concentration of 10 %. RAW 264.7 were grown in DMEM (Gibco, Boston, MA, USA) supplemented with 4.5 g L^{-1} glucose and 10 % FBS (Gibco, Boston, MA, USA). Both cells were cultured at 37 °C in a humidified incubator with 5 % CO_2. Cells were used only when mycoplasma was confirmed negative, and short-tandem repeat (STR) analysis was used to ensure cell line identities.

Preparation and characterization of nanoparticles: The DOX-oHA-PLN was synthesized using a previously developed one-pot self-assembly technique [28]. Briefly, a mixture of 25 mg of ethyl arachidate, 2 mg of Polyoxyethylene (40) stearate, and 1 mg of Polyoxyethylene (100) stearate was melted in a 15 mL conical tube in a 60 °C water bath. When all the lipids had melted, 100 μL of oHA (stock: 100 mg mL^{-1}), 250 μL of DOX (stock: 10 mg mL^{-1}), and 50 μL of Pluronic® F-68 (PF-68) (stock: 100 mg mL^{-1}) were added to the tube and stirred for 20 min. All solutions were prepared in distilled deionized (DDI) water. The nanoparticle suspension was emulsified for 5 min at 60 °C using a Hielscher UP 100H probe ultrasonicator at 100 % peak power (Ringwood, NJ, USA). After sonication, the formed nanoparticle emulsion was quickly transferred into 2.0 mL of saline or 5 % dextrose and mixed on ice to produce DOX-oHA-PLN. To prepare iRGD-conjugated DOX-oHA-PLN (iRGD-DOX-oHA-PLN), Myrj59-iRGD was synthesized, characterized, and added together with the PEG-lipid following the same procedure as for making DOX-oHA-PLN [28]. To prepare nanoparticles without oHA (i.e., DOX-PLN and iRGD-DOX-PLN), hydrolyzed polymers of epoxidized soybean oil (HPESO) were employed to load DOX [28]. The same procedure was used to make nanoparticles without DOX, oHA, or both in the following particles (oHA-PLN, iRGD-oHA-PLN, or iRGD-PLN). The size and zeta potential of the nanoparticles were measured using a Malvern Zetasizer Nano ZS (Worcestershire, UK). To remove unencapsulated DOX and oHA, the co-loaded nanoparticle suspensions were centrifuged at 8000×g for 15 min using a 0.1 μm centrifugal filter unit (Millipore, Etobicoke, ON, Canada). The concentrations of free DOX and oHA in the filtrate were quantified using spectrophotometry (Molecular Devices, San Jose, CA, USA) and gel permeation chromatography (GPC), respectively. These values were used to calculate the drug loading content (expressed as % w/w of encapsulated drug relative to the total nanoparticle weight) and encapsulation efficiency (expressed as % w/w of encapsulated drug relative to the total drug initially added).

Determination of synergism of DOX and oHA: To determine the optimized DOX:oHA ratio, 4T1-luc cells in 100 μL of growth medium were plated at a density of 1×10^4 cells per well in 96-well plates and incubated for 18 h. The cells were then treated with solutions of DOX and oHA at mass ratios of 1:0, 1:1, 1:2, 1:4, 1:6, 1:8, or 1:10 at a constant DOX concentration of 0.1 μg mL^{-1} for 24 h. Cell viability was measured using the MTT assay. For the MTT assay, 100 μL of 1 mg mL^{-1} MTT in RPMI medium (no serum) was added to each well, followed by 4 h of incubation at 37 °C. Then, 100 μL of dimethyl sulphoxide (DMSO) was added to each well and plates were incubated for another 30 min at 37 °C to dissolve formazan. The absorbance of formazan solution was measured with a SpectraMax M2 microplate reader (Molecular Devices, Sunnyvale, CA) at 562 nm. The determined DOX:oHA mass ratio was used for all subsequent *in vitro* and *in vivo* evaluations.

The MTT assay was also utilized to evaluate the synergistic effect between DOX and oHA and the cytotoxicity of the iRGD-DOX-oHA-PLN formulation.

To evaluate the drug synergy between DOX and oHA, 4T1-luc cells were seeded in 96-well plates at a density of 1×10^4 cells per well and incubated for 18 h. The cells were then treated for 24 h with either free drug solutions or nanoparticle formulations of DOX, oHA, or their combination at DOX concentrations ranging from 0.01 to 50 μg mL^{-1} and corresponding oHA concentrations at four times the DOX equivalence (0.04–200 μg mL^{-1}). Cell viability was assessed using the MTT assay as previously described. The subsequent synergy analysis adopted the Chou-Talalay method [29]. The median effect plot and combination index (CI) plot were generated based on the cytotoxicity of DOX and oHA alone or in combination. The CI values < 1, = 1, and >1 indicate synergism, additive effect, and antagonism, respectively. The median effect analysis involved plotting the log $\left[(f_a)^{-1} - 1\right]^{-1}$ versus log $[D]$ for DOX alone, oHA alone, and their combination, where f_a is the fraction of cells affected, and D is the drug concentration. The slope (m), indicating sigmoidicity, and the median effect dose (D_m) were derived from the fitted plot. The doses of the individual drugs and the drug combination (D_{x1}, D_{x2} and $D_{x1,2}$) that affect a given percent (%) of the plated colonies were calculated using the following equations:

Eq 2:

$$D_x = D_m \left[\frac{f_a}{1 - f_a}\right]^{1/m}$$

Based on Eq (2), the CI was calculated from.

Eq 3:

$$CI = \frac{D_1}{D_{x1}} + \frac{D_2}{D_{x2}} + \frac{D_1 D_2}{D_{x1} D_{x2}}$$

In vitro cellular uptake of DOX: oHA was covalently conjugated to cyanine 5 (Cy5) amine (Lumiprobe, Hunt Valley, MD, USA) via NHS/EDC coupling to generate Cy5-oHA. The uptake of DOX and Cy5-oHA by 4T1-luc cells was examined using confocal microscopy. Cells were seeded at a density of 3×10^5 cells in 3 mL of growth media 35 mm glass-bottom culture dishes (MatTek Corporation, Ashland, OR, USA). Cells were treated with free DOX + oHA, DOX-oHA-PLN, or iRGD-DOX-oHA-PLN for 1 h. Hoescht 33342 was added for nuclear staining 10 min before removing the medium and fixation with 1 % paraformaldehyde. Post-fixation and triple washing with PBS, the cells were imaged using a Leica TCS SP8 confocal microscope (Advanced Optical Microscopy

Facility in Toronto, CA). The excitation wavelengths used were 405 nm (blue, for Hoechst 33342), 488 nm (green, for DOX), and 638 nm (red, for Cy5-oHA).

Cells were plated in 6-well plates at a density of 2×10^5 cells per well and incubated at 37 °C. Upon reaching 80 % confluency, suspensions of free DOX + oHA, DOX-oHA-PLN, or iRGD-DOX-oHA-PLN were added to each well at 15 μg mL^{-1} DOX concentration. At predetermined time intervals (0–2 h), supernatants were removed, and cells were washed with ice-cold PBS and lysed with PBS containing 0.5 % Triton X-100. The cell lysates were then transferred to a 96 black-well plate for DOX concentration measurement using a SpectraMax Gemini XS microplate fluorometer (Molecular Devices, Sunnyvale, CA; excitation wavelength 480 nm, emission wavelength 590 nm). A standard curve with known DOX concentrations was used to calculate the DOX levels in the cell lysates. Cellular DOX concentration was normalized to protein concentrations, which were determined by the bicinchoninic acid (BCA) colorimetric assay (Thermo Scientific, Waltham, MA, USA). Bovine serum albumin provided by the manufacturer was used to plot the standard curve.

In vitro anti-migration and anti-invasion assays: For transwell migration or transwell invasion assays, 4T1-luc cells were plated in T25 tissue culture flasks (Sarstedt, Saint Léonard, QC, CA) at a density of 1×10^6 and were treated with saline, iRGD-PLN, free oHA, oHA-PLN, or iRGD-oHA-PLN at an oHA concentration of 10 μg mL^{-1} for 24 h. Cells were then trypsinized and transferred to the upper chamber of the transwell apparatus (Corning, New York, USA) in RPMI medium without serum. Cell inserts (8.0 μm pore size) were pre-coated with 100 μL Matrigel® Matrix (Corning, New York, USA) for the invasion assay before cell seeding. The lower chamber was filled with a growth medium containing 10 % FBS that acts as chemoattractant to facilitate cell migration or invasion over a 24-h period. Cells remaining on the upper surface of the insert were gently removed with cotton swabs. The cells that migrated or invaded the bottom surface were fixed with 4 % paraformaldehyde and stained with 0.5 % crystal violet. Images of the bottom of the insert were captured using the EVOS XL Core imaging system (Thermo Fisher Scientific, Inc., Waltham, MA, USA). The migrated or invaded areas were quantitatively analyzed using Image J software.

Wound healing assays were conducted to assess the *in vitro* anti-migration effect of iRGD-oHA-PLN on 4T1-luc cells. For this assay, 4T1-luc cells were seeded in 24-well plates at a density of 2×10^5. Upon reaching 100 % confluence, the cell monolayers were scratched using a 100 μL pipette tip and then rinsed twice with PBS. Following this, the cells were treated with saline, iRGD-PLN, free oHA, oHA-PLN, or iRGD-oHA-PLN, all at an oHA concentration of 30 μg mL^{-1}. After 24 h, the plates were rinsed twice with PBS, and images of the scratched areas were captured using an AMG EVOS FL fluorescence microscope (Thermo Fisher Scientific, Inc., Waltham, MA, USA).

ATP and HMGB1 release study: To evaluate ATP and HMGB1 released from 4T1-luc cells, the cells were seeded into 6-well plates at a density of 1×10^5 per well and incubated for 18 h to allow for growth. The cells were treated with either saline, free DOX + oHA, DOX-oHA-PLN, or iRGD-DOX-oHA-PLN, all at an equivalent DOX concentration of 0.5 μg mL^{-1} for 1 h. Following this treatment, the media were replaced, and the cells were incubated for 24 h. After the incubation, the supernatant was collected, and the ATP level was measured using an ATP Bioluminescence Assay Kit and HMGB1 by and HMGB1 ELISA kit.

Calreticulin expression: 4T1-luc cells were seeded in 35 mm glass-bottom culture dishes and allowed to grow for 18 h. They were treated with free DOX + oHA, DOX-oHA-PLN, or iRGD-DOX-oHA-PLN at an equivalent DOX concentration of 0.5 μg mL^{-1} for 1 h. After treatment, the cells were washed with PBS and fixed with cold 100 % methanol for 5 min. Following fixation, the cells were blocked overnight with blocking buffer (1 % BSA, 0.3 M glycine, and 10 % FBS in PBS) at 4 °C. Subsequently, the cells were incubated with Alexa Fluor® 647 anti-calreticulin antibody at a dilution of 1:500 for 24 h at 4 °C. After incubation, the cells were washed three times with PBS and were stained with Hoechst 33342 nuclear stain for 15 min at a concentration of 2 μg mL^{-1} at 37 °C. Finally, the cells were imaged using CLSM at specific wavelengths for Hoechst 33342 (405 nm) and Alexa Fluor 647 (650 nm).

Mouse tumor model: The *in vivo* efficacy studies were performed using 6-8-week-old female BALB/c mice. To establish the model, cells were orthotopically inoculated into mice by implanting 5.0×10^5 cells suspended in RPMI medium into the right fourth mammary fat pad of mice (The Jackson Laboratory, USA). Animals were provided food and water ad libitum for the entire duration of the experiments.

Animal tissues: Major organs and tumor tissue were obtained through surgical resection from inoculated mice that underwent surgery in the UHN Cancer Center (Toronto, Canada). All materials were collected according to national and institutional guidelines (Research Ethics Committee approval (AUP: 4333).

Animal tumor model: All animal handling and experimental procedures were conducted under protocols approved by the Animal Care Committee of the University Health Networks (UHN, Toronto, ON, Canada). The orthotopic metastasizing TNBC tumor model of mouse 4T1-luc cells was used for all *in vivo* studies. To establish the model, cells were orthotopically inoculated into mice by implanting 5×10^5 cells suspended in RPMI medium into the right 4th mammary fat pad of 6-8-week-old female BALB/c mice (The Jackson Laboratory, USA). Before injection, the cells were grown to 50–80 % confluency and trypsinized. Their viability was assessed using 0.4 % trypan blue using the hemacytometer. The bioluminescent luciferase-expressing 4T1-luc cells were used for *in vivo* lung metastasis monitoring via luciferin-induced bioluminescence imaging using a Xenogen IVIS spectrum imager (Caliper Life Sciences, Hopkinton, MA, USA). Luciferin solutions (15 mg mL^{-1}, 200 μL per mouse) were prepared in PBS and were administered to mice via intraperitoneal injection 10 min before imaging. The dose of doxorubicin was set at the maximum tolerated dose of 10 mg kg^{-1}, and the timing of sacrifice for the mice varied depending on the specific objectives of the experiments: 24 h after the first treatment for apoptosis studies, 5 days after the first treatment for immune marker studies, and 2 weeks after the second treatment for evaluating treatment efficacy and metastasis monitoring. Tumor sizes were monitored weekly for up to 8 weeks using vernier calipers to measure in two dimensions. The following formula was used to calculate tumor volumes:

$$V = \frac{\left[(length) X \, (width)^2\right]}{2}$$

In vivo biodistribution study: oHA was covalently linked to the near-infrared dye Cy7 (Lumiprobe, Hunt Valley, MD, USA) through EDC/NHS coupling to generate Cy7-oHA. Cy7-labeled nanoparticles were synthesized following the established protocol for non-fluorescently labeled nanoparticles, with the modification that oHA was substituted with Cy7-oHA. Mice bearing 4T1 orthotopic breast tumors were injected with 200 μL of the Cy7-labeled DOX-oHA-PLN or iRGD-DOX-oHA-PLN. The biodistribution of these nanoparticles was then investigated using *in vivo* whole-body and *ex vivo* organ fluorescence imaging. Specifically, whole-body *in vivo* biodistribution of the nanoparticles was monitored at designated time points for up to 72 h post-injection, using excitation and emission wavelengths of 745 nm and 820 nm, respectively. Critical organs such as the liver, spleen, kidneys, heart, and lungs were excised from and immediately imaged 24 h post-injection. The fluorescence intensities were quantified using the Living Image software, focusing on the region of interest (ROI). Fluorescence signals from the Cy7-labeled NPs in major organs were quantified and are presented as fold-changes from their respective background signals.

Accumulation of doxorubicin in primary tumors: BALB/c animals were orthotopically inoculated with 5×10^5 cells and monitored for 2–3 weeks until tumor sizes reached approximately 200 mm^3. The animals were then injected with 200 μL of free drug solutions or nanoparticles intravenously at an equivalent DOX dose of 10 mg kg^{-1}. Four hours post-injection, the animals were sacrificed, and the tumors were immediately harvested, embedded in Optimal Cutting Temperature (OCT) compound (Tissue-Tek, Torrance, CA, USA), flash-frozen in liquid nitrogen, and stored at −80 °C.

Tumor-containing tissue sections, sliced to a thickness of 10 μm using a microtome, were counter-stained with DAPI at the Pathology Research Center, UHN (Toronto, Canada) for fluorescence image analysis. To visualize blood vessels in the tumor sections, slides were successively labeled with anti-CD31 primary antibody and Alexa Fluor 647-conjugated goat anti-rat IgG secondary antibody (Abcam, USA). Slides were imaged with an Olympus Upright BX50 microscope equipped with a 100 W HBO mercury light source and Olympus UplanSApo 10X/0.40 objective lenses. The excitation and emission wavelengths for DOX and CD31 were 480/570 nm and 650/665 nm, respectively. The DOX-positive regions within the tumor were analyzed using HALO™ Image Analysis Software (PerkinElmer, Waltham, MA, USA). A minimum intensity threshold was set below the detectable DOX signal to minimize noise from tissue autofluorescence.

Immunohistochemical and immunofluorescence analysis: To analyze apoptotic biomarkers in 4T1-luc tumors, mice were intravenously injected with saline, free DOX, free DOX + oHA, iRGD-DOX-PLN, or iRGD-DOX-oHA-PLN three weeks after tumor cell inoculation. Tumors were excised 24 h post-treatment and immunohistochemically or immunofluorescently stained for apoptotic markers, including cleaved-caspase-3, TUNEL, γH2AX, and Ki67. The percentage of positively stained cells was quantified using HALO™ Image Analysis Software.

To analyze immune markers, tumors and major organs, including breast tumors, liver, lung, kidneys, and heart, were excised 5 days post-treatment. Tumor tissues were bisected, with one half used for immune marker assessment and the other for cytokine analysis. Tumor slices were fixed in 10 % neutral-buffered formalin, embedded in paraffin, and sectioned at 4 μm thickness using a microtome for subsequent analysis. Tumor slices were stained with antibodies against human CD8, CD4, granzyme B, F4/80, and FoxP3. Different organs were examined for signs of cellular toxicity using H&E staining. These analyses were conducted at the CFIBCR Histology/Microscope Core Unit (Toronto, ON, Canada).

Determination of cytokine IL-6: To evaluate IL-6 levels in the supernatants of co-cultured 4T1-luc cells and RAW 264.7 macrophages, both cell types were mixed at a 1:1 ratio and seeded at a density of 1×10^5 in a 50 % RPMI and 50 % DMEM complete growth media mixture. After 24 h, the supernatants were collected for IL-6 measurement. Subsequently, the cells were washed and imaged under a bright field using the inverted microscope EVOS XL Core imaging system (Thermo Fisher Scientific, Inc., Waltham, MA, USA).

To measure IL-6 levels in the supernatants of 4T1-luc cells, the other half of the tumors described in “Immunohistochemical and Immunofluorescence Analysis” were used. The tissues were freshly minced and placed into tissue lysis buffer containing 10 mM Tris-HCl, 150 mM NaCl, 1 % NP-40, 10 % Glycerol, 5 mM EDTA, and a protease inhibitor cocktail. The tissue samples were then homogenized using a microtube homogenizer (Fisher Scientific, Ontario, Canada), followed by a 1-h incubation at 4 °C with gentle agitation. The lysates were further processed with 20 s of sonication using a UP100H probe ultrasonicator (Hielscher Ultrasonics, Teltow, Germany) at 50 % amplitude. The samples were centrifuged at 15,000×*g* for 20 min at 4 °C. The supernatants were collected, and aliquots were stored at −80 °C for later use. The cytokine levels were determined using ELISA kits, following the manufacturers instructions. A BCA assay was performed to ensure uniform protein concentrations before the cytokine measurements.

In vivo anti-tumor and anti-metastasis effect: Approximately three weeks after tumor inoculation, when breast tumors reached a size of ~200 mm^3, mice were intravenously injected with saline, free DOX, free DOX + oHA, iRGD-DOX-PLN, or iRGD-DOX-oHA-PLN. All treatments were administered at an equivalent DOX concentration of 10 mg kg^{-1}. The mice received a second identical treatment two weeks following the first dose. The size of the breast tumors was monitored weekly using a vernier caliper. Spontaneous metastasis to the lungs was tracked weekly through bioluminescence imaging of the tumors using the Xenogen IVIS system (Caliper Life Sciences, Hopkinton, MA, USA). For this purpose, luciferin at 150 mg kg^{-1} was injected intraperitoneally 10 min before imaging. By the fourth week, distal metastases were identified by dissecting lungs and major organs from the sacrificed mice. These organs were immediately fixed in 10 % buffered formalin to assess metastatic burden. The lungs were sectioned coronally and stained with H&E at the CFIBCR Histology/Microscope Core Unit (Toronto, ON, Canada). The extent of distal metastases was quantified using HALO™ Image Analysis Software.

In a subset of animals, mice were sacrificed at the same endpoint, and their lungs were collected and minced to generate single-cell suspensions. These suspensions were prepared in 4T1-luc cell culture media containing 6-thioguanine to select 6-thioguanine-resistant 4T1-luc cells. After several media replacements, the formed cell colonies were fixed with 4 % paraformaldehyde. Subsequently, they were stained with 0.5 % crystal violet and visualized through bright field imaging using the EVOS XL Core imaging system. The number of cell colonies was counted.

Bioinformatic analysis: BC-GEM (Gene Expression Metastasis) database (https://bcgenex.ico.unicancer.fr/BC-GEM/GEM-Accueil.php) [30] is a specialized tool for analyzing breast cancer gene expression, focusing on metastasis. We employed BC-GEM to examine the expression levels of CD8A, CD4, ADGRE1, and IL6 in samples from TNBC patients, incorporating clinical parameters such as ER, PR, and HER2 status. Prognostic significance was evaluated using Kaplan-Meier survival analysis, which included hazard ratios (HR) and 95 % confidence intervals (CI). Correlations between gene expression and disease-free survival (DFS) were analyzed, with statistical significance determined by log-rank tests ($p < 0.05$).

Statistical analysis: All quantitative data are presented as mean ± standard deviation (SD). Students t-test or one-way analysis of variance (ANOVA) followed by Tukeys post hoc test were utilized to determine statistical significance between two or more groups. All statistical tests were conducted using GraphPad Prism software (San Diego, California, USA). P values < 0.05 were considered significant.

3. Results and discussion

3.1. Design of synergistic DOX and oHA combination nanoparticles against 4T1-luc cells

We first investigated the effect of DOX and oHA combination ratio on the viability of 4T1-luc murine TNBC cells using the MTT assay, with a fixed DOX dose of 0.1 μg/mL, to identify the optimal ratio. The results showed that cell viability significantly decreased as the DOX:oHA mass ratio was reduced to 1:4; however, further reduction beyond this ratio did not result in additional cytotoxicity (Fig. S1). Given the molecular weight of repeating unit of oHA as 379.32 Da and molecular weight of DOX at 543.52 Da, the mass ratio is translated to a molar ratio of DOX: oHA at 1:5.73. The excess amount of oHA ensures complete complexation of DOX with oHA enabling high drug loading efficiency. Considering the optimized DOX loading and favorable physicochemical properties of the nanoparticles, the 1:4 wt ratio was selected for all subsequent experiments involving both free DOX + oHA combination and their corresponding nanoparticle formulations. The particle size, polydispersity index (PDI), and zeta potential of various nanoparticle formulations are summarized in Fig. S2A–C, while encapsulation efficiency and drug loading content for DOX and oHA are summarized in Fig. S2D. As reported in our previous work, the nanoparticles were spherical; and the binding affinity of iRGD-DOX-oHA-PLN was confirmed using a binding assay with recombinant human αvβ3 integrin receptors [14,28]. The colloidal stability in 5 % dextrose or 50 % FBS as well as storage stability of the nanoparticle formulations were also demonstrated in our previous studies [14,28].

The synergistic cytotoxic effects of DOX and oHA, administered either as free drugs or co-encapsulated within polymer-lipid nanoparticles (PLNs), were assessed through cell viability and dose-response analyses, as illustrated in Fig. 2A and B. We evaluated the synergism of DOX and oHA combination at 1:4 ratio in 4T1-luc cells treated with DOX and oHA either as free solutions or encapsulated in nanoparticles (PLNs). From the cell viability-dose response curves determined by the MTT assay, the IC50 and combination indices of various treatment groups were evaluated. The IC50 of free DOX was found to be 5.9 ± 1.5 μg mL^{-1}, which decreased to 2.9 ± 0.91 μg mL^{-1} when combined with oHA (Fig. 2B). Nanoparticle treatments with DOX-PLN and DOX-oHA-PLN exhibited significantly higher cytotoxicity compared to their free drug counterparts, with IC50s of 2.1 ± 0.31 μg mL^{-1} and 0.44 ± 0.12 μg mL^{-1}, respectively (Fig. 2B). Median effect analysis and combination index (CI) calculations indicated a strong synergism between DOX and oHA in both free and nanoparticle forms. The synergistic effect of oHA with DOX is attributable partly to the pH-dependent ionic complexation between the two, which facilitates cellular uptake of DOX, lysosomal escape upon dissociation of DOX-oHA at acidic pH, and transport of DOX to nucleus [31–33] in addition to oHA-mediated sensitization of cancer cells to DOX via various signal pathways as elaborated in the following section.

The iRGD-functionalized DOX-oHA nanoparticles exhibited even lower IC50 value of 0.27 ± 0.09 μg mL^{-1} (Fig. S3A). The enhanced DOX uptake resulted in the higher anti-cancer effect of DOX shown *in vitro*. The iRGD-DOX-oHA-PLN nanoparticles effectively reduced the viability of 4T1-luc cells by ~6 times compared to free DOX. These results were further corroborated by crystal violet staining (Fig. S3B), where iRGD-DOX-oHA-PLN treatment showed the greatest reduction in cell density and viability using crystal violet staining, consistent with the IC50 and synergism data.

3.2. Integrin-targeted nanoparticles enhance cellular uptake of DOX, in vitro efficacy, and tumor accumulation in 4T1-luc model

In vitro cellular uptake of DOX was evaluated using confocal laser scanning microscopy (CLSM) and a spectrofluorometric assay. For these studies, nanoparticles were prepared with cyanine 5 (Cy5) dye-labeled oHA. The 4T1-luc cells were incubated at 37 °C for 1 h with either the free or the nanoparticle drug combination, with or without iRGD, and then imaged using CLSM (Fig. 2C). The CLSM images revealed highest uptake of both DOX and oHA-Cy5 in cells treated with iRGD-DOX-oHA-PLN, as indicated by intense nuclear staining of DOX and cytosolic distribution of oHA.

In time-dependent drug uptake studies, 4T1-luc cells treated with equivalent concentrations of DOX (either as the free drug combination or as nanoparticle formulations, with or without iRGD) were tested at intervals of 15, 30, 60, and 120 min using a fluorescence signal (BioTek Cytation 5). Intracellular DOX concentrations, normalized against total cellular protein concentrations (BCA protein assay), were reported as drug uptake per protein concentration (Fig. 2D). The nanoparticle formulations, both iRGD-targeted and non-targeted, showed higher DOX uptake than the free drug as early as 15 min post-treatment. At 2 h, the iRGD-DOX-oHA-PLN treatment exhibited a significant ~1.6-fold higher uptake of DOX compared to the non-targeted nanoparticle and a ~3.4-fold increase relative to the free DOX + oHA combination.

In vivo drug uptake experiment, BALB/c mice bearing tumors were sacrificed 4 h post i. v. Injections of free DOX + oHA, DOX-oHA-PLN, or iRGD-DOX-oHA-PLN. Tumors were collected for drug accumulation analysis. The iRGD-DOX-oHA-PLN treated group showed substantial DOX penetration and retention in the tumor compared to the free drug combination or the non-iRGD targeted nanoparticle combinations, which signifies the tissue-penetrating capability and high affinity of iRGD for integrins overexpressed on TNBC and tumor neovasculature [34,35]. Quantitative analysis of the DOX-positive area in tumor tissues revealed significantly higher DOX accumulation in mouse tumors treated with iRGD-DOX-oHA-PLN compared to free DOX + oHA, with a ~3.3-fold increase from 5 % to 19 % (Fig. 2E). Together, these results highlighted the enhanced specificity and prolonged tumor retention of iRGD-DOX-oHA-PLN, suggesting a sustained anti-tumor effect and reduced toxicity to normal tissues.

3.3. oHA and iRGD containing NPs significantly inhibit TNBC cell migration and invasion in vitro

To evaluate the impact of oHA and iRGD-containing formulations on 4T1-luc cell motility, we conducted transwell migration, transwell invasion, and wound healing assays. These tests were performed by treating the cells with various formulations containing iRGD and oHA, either individually or in combination. In the transwell assays, the iRGD-oHA-PLN formulation demonstrated significant inhibition of cancer cell migration and invasion, in contrast to the moderate effects observed with oHA-PLN and free oHA (Fig. S4).

In wound-healing assays, the naked iRGD-PLN significantly reduced cancer cell migration in the wound healing assay (Fig. S5), likely due to disruption of integrin signaling pathways, as supported by other studies [39]. Furthermore, the iRGD-oHA-PLN treatment notably inhibited cell migration into the scarred area. The percentage of the area recovered using was quantified with ImageJ. Notably, the iRGD-oHA-PLN treatment resulted in a 42 % reduction in the wound closure area within 24 h, compared to a 61 % reduction observed with the iRGD-PLN treatment. This anti-migratory effect of oHA is likely attributable to the disruption of native HA-RHAMM/ERK1/2 signaling pathways [28].

3.4. Drug distribution and tumor accumulation in mice bearing TNBC tumors

In complex living organisms, nanoparticles being administered must be able to "differentiate" between normal and tumor tissues. This specificity is crucial for ensuring that they successfully target and accumulate at the tumor site while minimizing toxicity to healthy tissues. To investigate *in vivo* drug distribution and accumulation, we utilized BALB/c mice bearing tumors and conducted the whole-body biodistribution analysis. Both *in vivo* and *ex vivo* analyses of various organs (heart, lung, liver, spleen, kidney, and tumor) were conducted to evaluate drug distribution following the treatment with nanoparticle drug combinations, with or without iRGD. To facilitate tracking, the near-infrared fluorophore cyanine 7 (Cy7) was used to label oHA (oHA-Cy7), which was then incorporated into the nanoparticles.

The biodistribution of these different formulations was monitored *in vivo* at 0, 1, 2, 4, 8, 24, 48, and 72 h post-treatment and analyzed using the Xenogen IVIS imaging system. Initially, at 1 h and 2 h post intravenous (i.v.) injection (10 mg kg^{-1} of DOX for all treatments), the nanoparticles were predominantly localized in the abdominal area of the animals. Starting from hour 4, a noticeable shift of the nanoparticles signal was shown to head towards the primary tumor site. The signal was retained for over 48 h in the animals treated with iRGD-DOX-oHA-PLN compared to the non-iRGD functionalized particles (Fig. S6A). Representative *ex vivo* images of the major organs and tumors were excised from mice that are sacrificed 24 h post-treatment, revealing that the iRGD-DOX-oHA-PLN significantly enhanced tumor drug uptake by approximately 2.2-fold compared to the non-targeted DOX-oHA-PLN (Fig. S6B).

3.5. Enhanced tumor apoptosis by iRGD-DOX-oHA-PLN

To evaluate the apoptotic and proliferative responses in mouse tumors subjected to various treatments, BALB/c mice bearing tumors (~200 mm^3) received treatments including saline, free DOX, free DOX + oHA, iRGD-DOX-PLN, or iRGD-DOX-oHA-PLN (10 mg kg^{-1} of DOX for all treatments). After 24 h following the intravenous injections, the animals were sacrificed, and primary tumors were excised for detailed immunohistochemical and immunofluorescence analyses. These

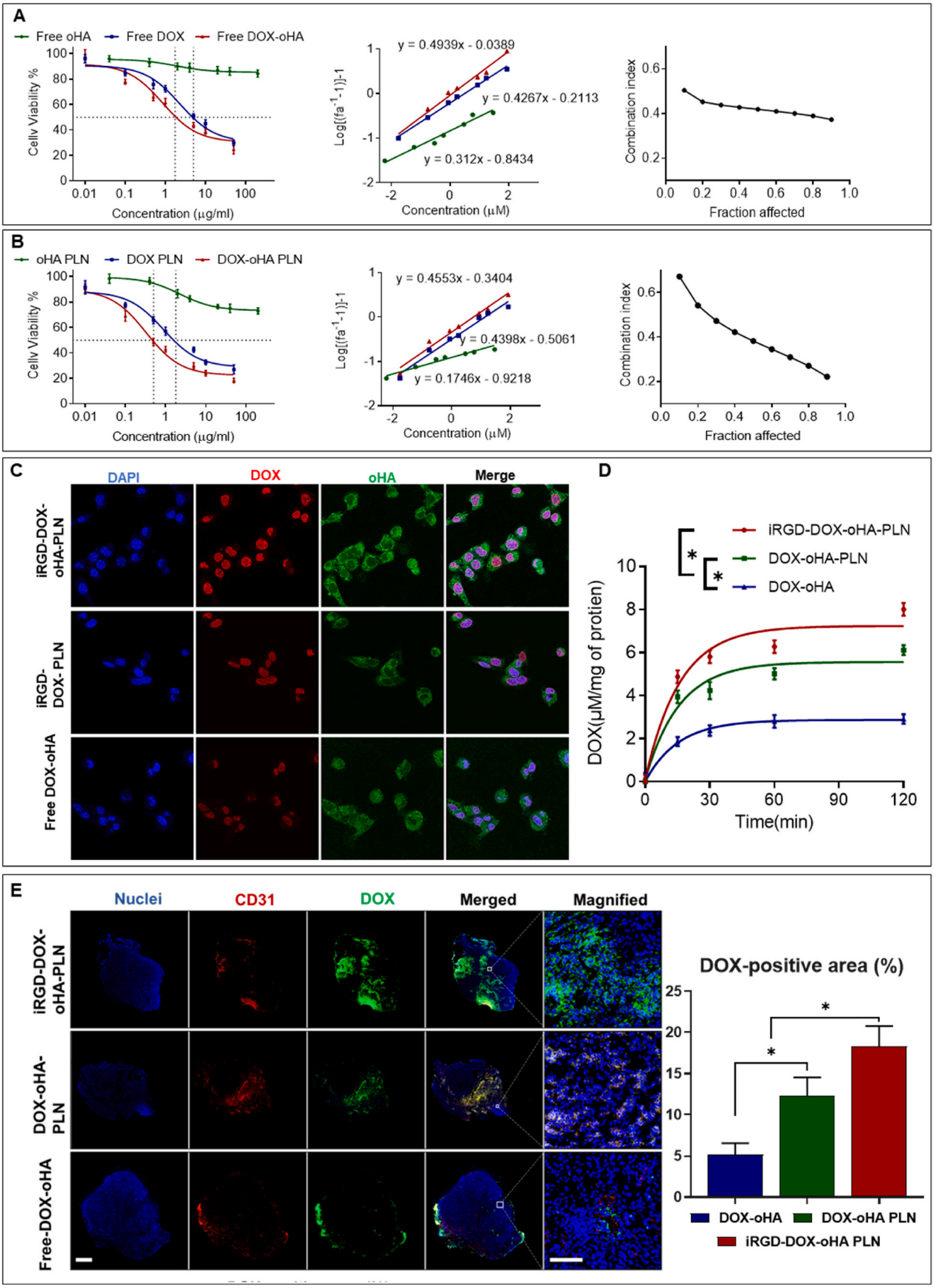

(caption on next page)

Fig. 2. iRGD conjugation enhances cellular uptake, tumor accumulation and penetration of nanoparticle delivered DOX. Dose-response curves, median effect plots, and CI analyses display the synergistic interaction between DOX and oHA in 4T1-luc TNBC cells. Cells were treated with **A)** free solutions containing oHA, DOX, or their combination, and **B)** nanoparticle formulations of oHA-PLN, DOX-PLN, and DOX-oHA-PLN, all at equivalent DOX concentrations ranging from 0.01 to 50 μg mL-1. All data are presented as mean ± standard deviation (SD) (n = 3), $^{**}p < 0.01$. **C)** CLSM images of 4T1-luc cells following a 1-h treatment with free DOX + oHA, DOX-oHA-PLN, or iRGD-DOX-oHA-PLN. Scale bar = 50 μm. **D)** Time-dependent DOX fluorescence in 4T1-luc cells treated with the same formulations, measured using a spectrofluorometer over 15 min to 2 h. The data are expressed as fold changes relative to the uptake of free DOX in 4T1-luc cells. **C)** Representative images showing the immunofluorescence staining (DAPI, CD31, DOX) of 4T1-luc orthotopic tumor sections. Scale bar = 2.5 mm for original images. Scale bar = 250 μm for magnified immunofluorescence images. **E)** Representative immunofluorescence images and quantification of DOX distribution in 4T1-luc orthotopic tumors 4 h after i. v. Administration of free DOX + oHA, DOX-oHA-PLN, or iRGD-DOX-oHA-PLN (10 mg/kg DOX-equivalent). Tumor sections were stained for nuclei (DAPI), vasculature (CD31), and DOX fluorescence. Scale bars: 2.5 mm (whole tumor); 250 μm (magnified regions). DOX-positive area (%) was quantified using HALO software from three sections per mouse (n = 3 mice/group). Data are presented as mean ± SD. $^{*}p < 0.05$.

analyses focused on assessing cell apoptosis (TUNEL and cleaved caspase-3), DNA damage (γH2AX), and cell proliferation (Ki67). Representative images of 4T1-luc tumor sections from the BALB/c mice, along with a quantitative biomarker analysis for these markers across the five treatment groups, are illustrated in Fig. 3.

It was observed that the group treated with iRGD-DOX-oHA-PLN exhibited the most significant induction of cell death and DNA damage, with approximately 51 % of cells showing TUNEL positivity, 47 % cleaved caspase-3 positivity, and 55 % γH2AX positivity. Correspondingly, the expression of Ki67, indicative of cell proliferation, was markedly lower (16 %) in this group (Fig. 3B). Tumors treated with iRGD nanoparticles demonstrated significantly elevated levels of apoptosis compared to those receiving the free drug treatment, highlighting the benefits of targeted delivery achieved through the iRGD-peptide. The synergistic combination of nanoparticle-formulated oHA and DOX in treating tumors was evident in all these markers compared to the DOX treatment alone.

3.6. *iRGD-DOX-oHA-PLN boost the antitumor immune response*

To assess whether the nanoparticle formulations can stimulate an anti-tumor immune response *in vivo*, we harvested orthotopic 4T1-luc tumors 5 days post-treatment for immunohistochemical (IHC) analysis of CD4, CD8, and granzyme B expression (Fig. 4). Emerging studies have highlighted the role of $CD4^+$ T cells in mounting an immune response against cancer cells via direct interactions with $CD8^+$ and antigen-presenting cells (APCs) [40]. Our results demonstrated a notable enhancement in intratumoral $CD4^+$ and $CD8^+$ T cell infiltration

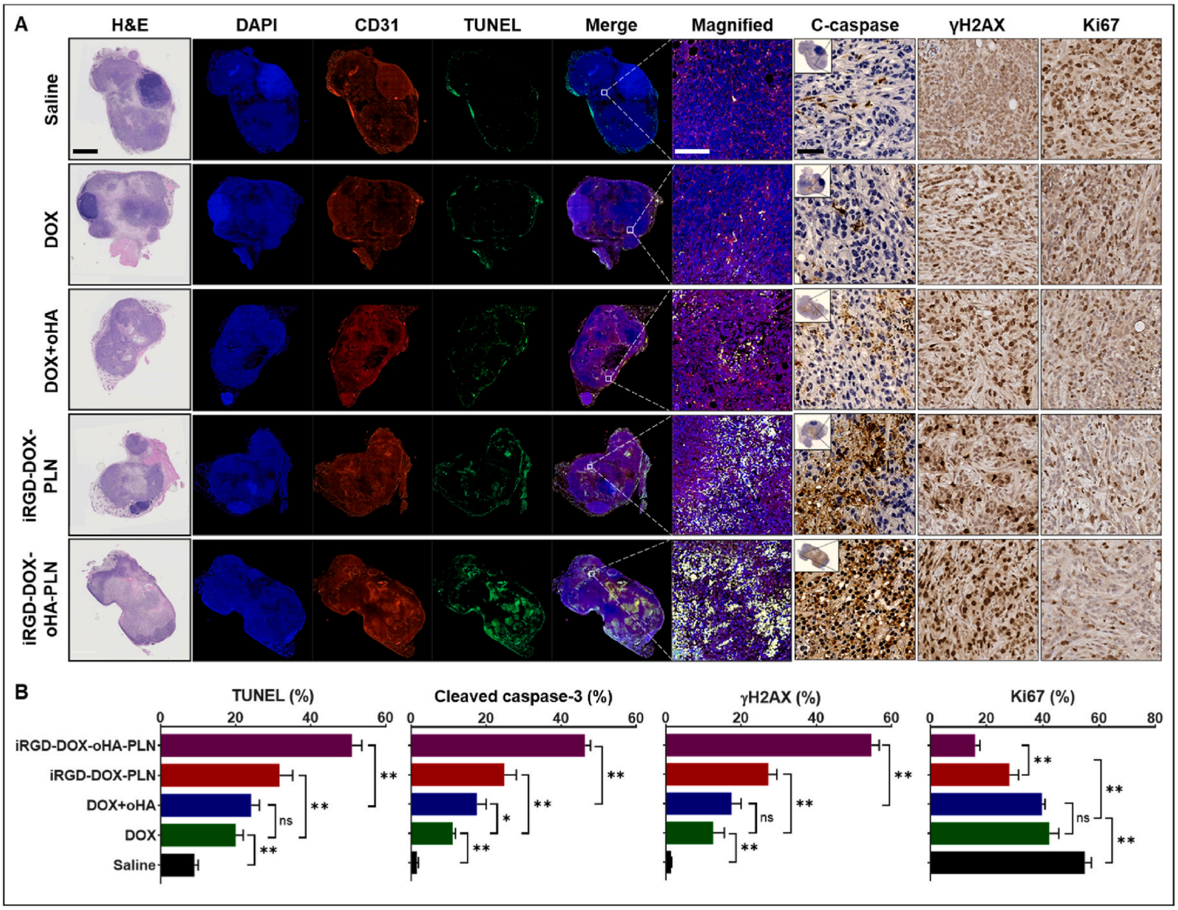

Fig. 3. iRGD-DOX-oHA-PLN enhance apoptosis, cell death and DNA double-strand break markers in 4T1-luc mouse tumors. A) Representative images showing the H&E staining, immunofluorescence staining (DAPI, CD31, TUNEL), and immunohistochemical staining (cleaved caspase-3, γH2AX, Ki67) of 4T1-luc orthotopic tumor sections. Tumors were excised from mice 24 h after i. v. Treatment with saline, free DOX, free DOX + oHA, iRGD-DOX-PLN, or iRGD-DOX-oHA-PLN, all administered at an equivalent DOX concentration of 10 mg kg^{-1}. Scale bar = 2.5 mm for original images. Scale bar = 250 μm for magnified immunofluorescence images. Scale bar = 50 μm for magnified immunohistochemical images. **B)** Quantitative analysis of stained sections. N = 3 sections per tumor in one mouse were used. N = 5 mice were used. All data are presented as mean ± SD. $^{*}p < 0.05$. $^{**}p < 0.05$.

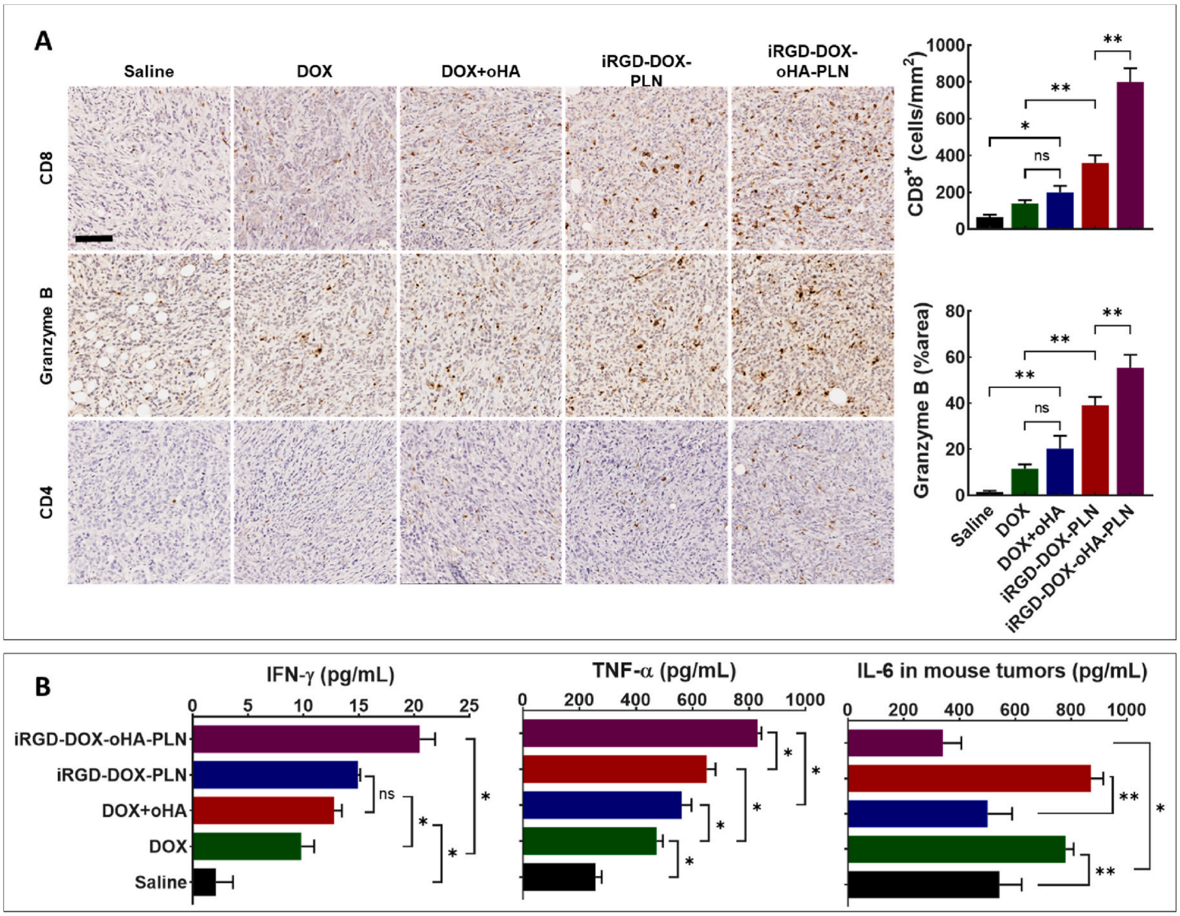

Fig. 4. iRGD-DOX-oHA-PLN induces anti-tumor immune cells in orthotopic 4T1-luc tumors. A) Immunohistochemistry and quantitative analysis of CD8, granzyme B, and CD4 in 4T1-luc tumors. Female BALB/c mice inoculated with orthotopic 4T1-luc tumors (300–400 mm^3) were treated with saline, free DOX, free DOX + oHA, iRGD-DOX-PLN, or iRGD-DOX-oHA-PLN (DOX 10 mg kg^{-1}) five days before sacrifice. Scale bar = 50 μm. N = 3 sections were used per mouse. N = 3 mice were used. **B)** Quantitative analysis of IFN-γ, TNF-α, and IL-6 levels in the same tumor samples by enzyme-linked immunosorbent assay (ELISA). N = 3. All data are presented as mean ± SD. $^*p < 0.05$. $^{**}p < 0.01$.

following treatment with nanoparticle formulations. Compared to free DOX, treatment with DOX + oHA resulted in a ~1.4-fold increase in CD4$^+$ T cells and a ~2.5-fold increase in CD8$^+$ T cells, indicating the immune-potentiating effect of oHA. Moreover, the iRGD-DOX-PLN group showed a ~2.5-fold increase in CD4$^+$ T cells and a ~5-fold increase in CD8$^+$ T cells compared to DOX. Notably, the iRGD-DOX-oHA-PLN group elicited the strongest immune response, with a ~3-fold increase in CD4$^+$ T cells and a ~8-fold increase in CD8$^+$ T cells compared to the DOX+oHA group. These findings underline the synergistic effect of combining oHA and iRGD-in a nanoparticle-based delivery system to remodel the immune TME (Fig. 4A).

A similar trend was observed in the increased secretion of granzyme B, a serine protease primarily produced by cytotoxic T cells, activated NK cells, and specific populations of activated CD4$^+$ T cells that mediates the apoptosis of target cells [19]. The treatments with iRGD-DOX-oHA-PLN and iRGD-DOX-PLN both significantly enhanced Granzyme B expression compared to their respective free drug counterparts. Specifically, iRGD-DOX-PLN induced a ~2.5-fold increase in Granzyme B release compared to free DOX, while iRGD-DOX-oHA-PLN led to a ~3.6-fold increase. Additionally, DOX-oHA alone exhibited ~2.8-fold higher Granzyme B expression than free DOX, indicating that oHA contributes to immune activation even without the nanoparticle carrier. Notably, iRGD-DOX-oHA-PLN produced a ~44 % increase in Granzyme B release compared to iRGD-DOX-PLN, highlighting the synergistic enhancement achieved by incorporating oHA into the nanoparticle formulation (Fig. 4A). This synergism is likely attributed to the combined effects of enhanced DNA damaging and the ICD-inducing properties of DOX, along with the activation of DCs by oHA, as reported others [12,38].

Moreover, tumor necrosis factor (TNF)-α, IFN-γ, and IL-6 are critical in modulating immune response towards inducing antitumor immune effects, were analyzed by ELISA in this study. Results from homogenized tumor tissues revealed that oHA-containing treatment (iRGD-DOX-oHA-PLN) significantly enhanced pro-inflammatory cytokine production compared to both free DOX and iRGD-DOX-PLN. Specifically, TNF-α and IFN-γ levels in the iRGD-DOX-oHA-PLN group were increased by approximately 2.7-fold and 2.5-fold, respectively, compared to free DOX. When compared to iRGD-DOX-PLN, the same formulation led to a ~36 % increase in TNF-α and a ~25 % increase in IFN-γ, suggesting that the addition of oHA further potentiates the immunostimulatory effects of nanoparticle-based chemotherapy in the TNBC tumor microenvironment (Fig. 4B). This elevation suggests enhanced dendritic cells (DCs) maturation and T-cell activation, likely resulting from the augmented capacity of iRGD-DOX-oHA-PLN to target tumor cells. The IL-6 levels in 4T1-luc mouse tumors increased following free DOX or DOX alone NP formulation treatment but significantly decreased when treated with oHA-containing formulations (Fig. 4B). Overall, these findings highlight the impact of iRGD-DOX-oHA-PLN in shaping the antitumor immune landscape and potentially improving the therapeutic outcomes against TNBC tumors.

3.7. iRGD-DOX-oHA-PLN inhibit the recruitment of immunosuppressive cells

Tumors often exploit Treg lymphocytes, MDSCs and M2-polarized macrophages, which are key immunosuppressive cell types within the TME, to evade immune responses [36]. We assessed the changes in $Treg^+$ cell numbers following various treatments through immunohistochemical analysis of FoxP3 expression (Fig. 5A and B). A consistent decrease in both $FoxP3^+$ and $CD11b^+$ cell numbers across all treatment groups was observed as compared to the saline control, with the most significant reduction (98 % for $FoxP3^+$ cells and 80 % for $CD11b^+$ cells) following the treatment with iRGD-DOX-oHA-PLN. This reduction is attributable to a dual mechanism of synergized cytotoxic effect of DOX and the potential modulation of PI3K signaling by oHA, as suggested by the comprehensive analysis of all treatment groups [37]. The observed reduction of $F4/80^+$ and $CD11b^+$ cells in tumors by the iRGD-DOX-oHA-PLN group suggests the depletion or infiltration-inhibition of the immunosuppressive myeloid populations, including potential MDSCs, within the TME. Moreover, the downregulation of CD206 and upregulation of CD86 in tumors treated by iRGD-DOX-oHA-PLN demonstrated that the DOX and oHA synergism induces macrophage polarization from anti-inflammatory M2 to pro-inflammatory M1, thereby enhancing anti-tumor immune response (Fig. S7).

3.8. Immunogenic Cell Death Induction and IL-6 suppression by iRGD-DOX-oHA-PLN

The enhanced drug delivery achieved through iRGD nanoparticles is likely to maximize the ICD induction by DOX, potentially leading to a more robust antitumor immune response. To evaluate the ability of the nanoparticles to induce ICD, we examined the expression of three key DAMPs, calreticulin, ATP and HMGB1. For the evaluation of calreticulin, 4T1-luc cells were treated for 1 h with free DOX-oHA, iRGD-DOX-PLN, or iRGD-DOX-oHA-PLN and subsequently imaged using CLSM. The results revealed the most pronounced calreticulin expression in cells treated with iRGD-DOX-oHA-PLN, as indicated by extensive fluorescent staining (Fig. 6A). Evaluation of supernatants of 4T1-luc cells under the same treatment condition showed ∼ 2-fold increase in ATP release after the iRGD-DOX-oHA-PLN treatment compared to free DOX-oHA (Fig. 6B). The HMGB1 levels increased by 17.5 % with iRGD-DOX-oHA-PLN treatment compared with free DOX-oHA (Fig. 6C). The significant induction of ICD, especially in cells treated with iRGD-DOX-oHA-PLN, is likely due to its enhanced cellular uptake and tumor targeting and penetration (Fig. 2).

Within the TME, tumor-associated macrophages (TAMs), predominantly characterized by the M2 phenotype, pose significant challenges to the effectiveness of cytotoxic chemotherapy by suppressing immune-mediated mechanisms [41]. To assess the *in vitro* efficacy of the

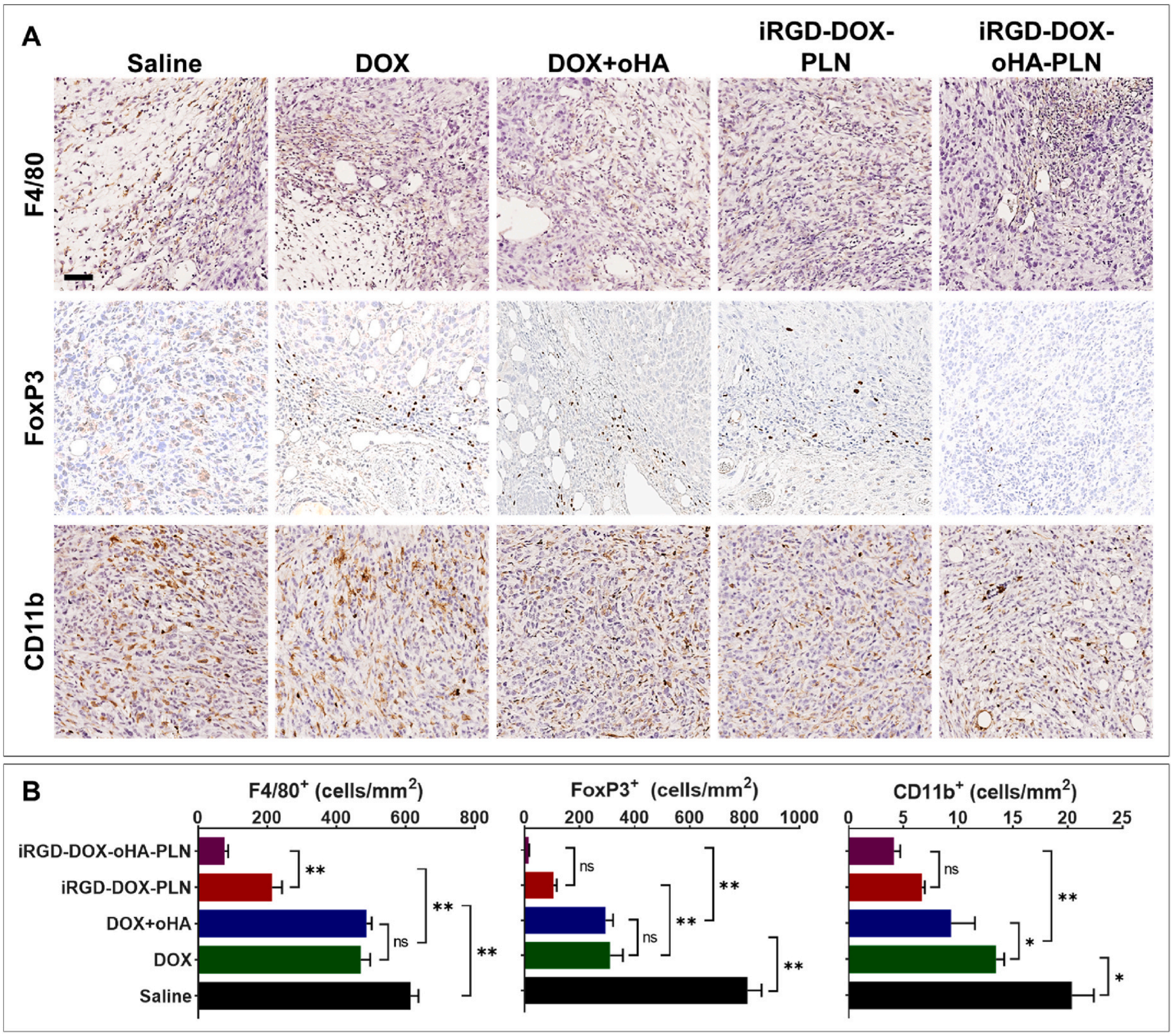

Fig. 5. The iRGD-DOX-oHA-PLN depletes the tumor immunosuppressive cells. A) Immunohistochemistry analysis of F4/80, FoxP3, and CD11b expression in tumor tissues from various treatment groups. Scale bar = 50 μm. **B)** Quantitative analysis of immunohistochemically stained sections of F4/80, FoxP3, and CD11b. N = 3 sections were used per mouse and n = 3 mice were used. All data are presented as mean ± SD. $^*p < 0.05$. $^{**}p < 0.01$.

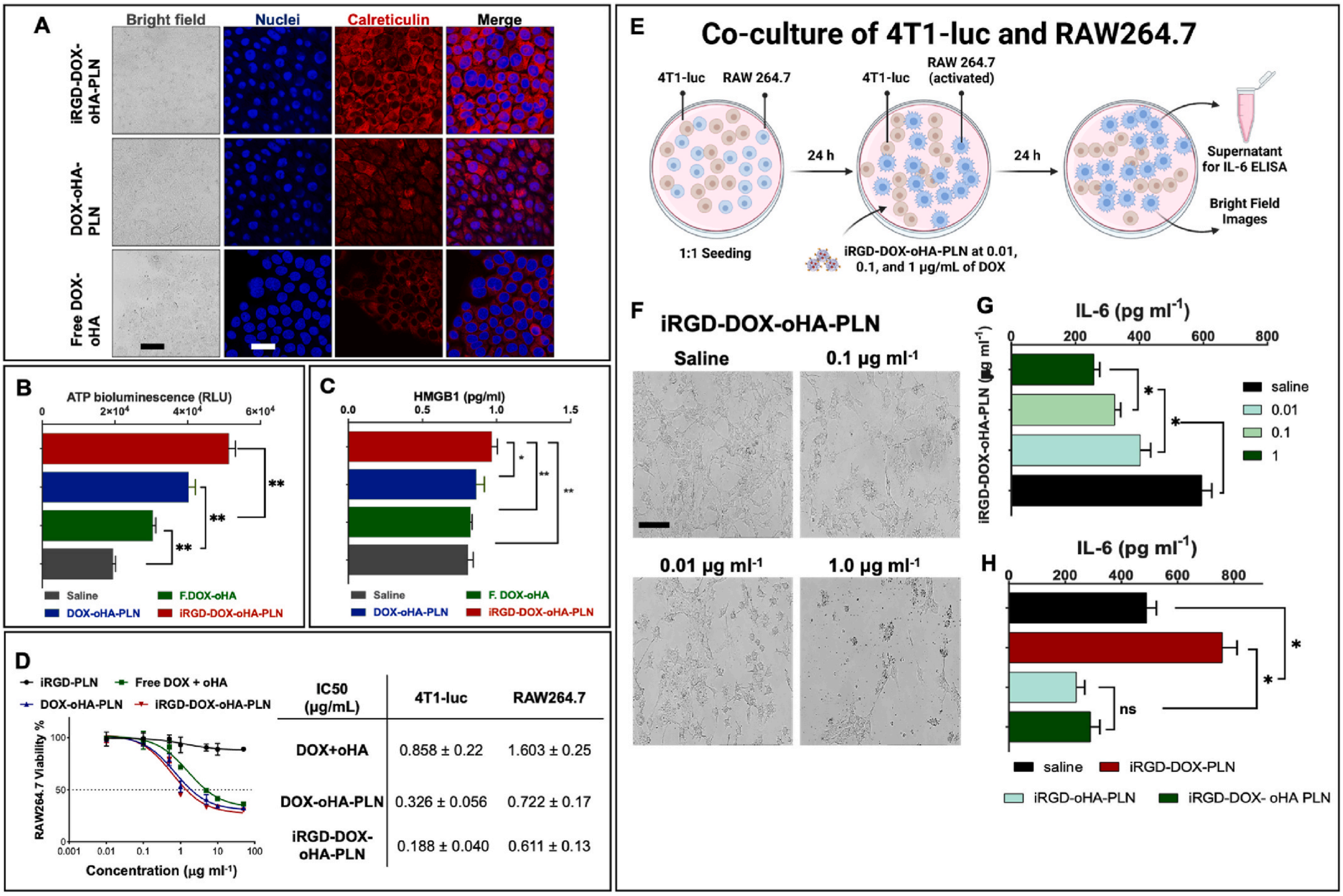

IC50 (μg/mL)	4T1-luc	RAW264.7
DOX+oHA	0.858 ± 0.22	1.603 ± 0.25
DOX-oHA-PLN	0.326 ± 0.056	0.722 ± 0.17
iRGD-DOX-oHA-PLN	0.188 ± 0.040	0.611 ± 0.13

Fig. 6. Immunogenic Cell Death Induction and IL-6 Suppression by iRGD-DOX-oHA-PLN in 4T1-luc Tumor Cells and Co-culture. A) CLSM images showing calreticulin expression in 4T1-luc cells. Cells were treated with free DOX + oHA, DOX-oHA-PLN, or iRGD-DOX-oHA-PLN at an equivalent DOX concentration of 0.5 μg mL^{-1}. Scale bar = 50 μm. **B)** ATP bioluminescence assay of 4T1-luc cell supernatants after treatments with saline, free DOX + oHA, DOX-oHA-PLN, or iRGD-DOX-oHA-PLN at an equivalent DOX concentration of 0.5 μg mL^{-1} (n = 3). **C)** Released HGBM1 by 4T1-luc cells treated with saline or various formulations (n = 3). **D) Left:** Cell viability of RAW 264.7 cells following 24 h of exposure to iRGD-PLN and three different DOX formulations (free DOX + oHA, DOX-oHA-PLN, and iRGD-DOX-PLN) at varying DOX concentrations (0.01–50 μg mL^{-1}). **Right:** A comparison of IC50 values of 4T1-luc cells and RAW 264.7 cell lines treated with DOX-containing nanoparticle formulations (n = 3). **E)** Schematic illustration of the co-culture model composed of 4T1-luc breast cancer cells and RAW 264.7 macrophages (1:1 ratio), treated with iRGD-DOX-oHA-PLN at varying DOX concentrations (0.01, 0.1, and 1.0 μg mL^{-1}) or saline. **F)** Brightfield images were acquired 24 h post-treatment using an EVOS XL microscope. Scale bar = 200 μm. **G)** Quantification of IL-6 levels in co-culture supernatants following treatment with iRGD-DOX-oHA-PLN at the indicated DOX concentrations for 24 h (n = 3). **H)** IL-6 levels in monocultured 4T1-luc cells treated for 24 h with saline, iRGD-DOX-PLN, iRGD-oHA-PLN, or iRGD-DOX-oHA-PLN at an equivalent concentration of DOX (0.5 μg mL^{-1}) or oHA (2 μg mL^{-1}), as appropriate (n = 3). All data are presented as mean ± SD, $^{*}p < 0.05$. $^{**}p < 0.01$.

iRGD-DOX-oHA-PLN nanoparticle formulation against macrophages, we performed MTT assay using murine RAW 264.7 cells. Notably, this formulation significantly increased the cytotoxicity of DOX compared to the free drug combination (Fig. 6D). Interestingly, both non-targeted and iRGD-targeted nanoparticles exhibited similar toxicities in RAW 264.7 macrophages, potentially due to their low integrin expression [42]. The IC50 values for both 4T1-luc and RAW 264.7 cell lines, as summarized in Fig. 6D, suggests that the macrophages are inherently more resistant to these formulations than 4T1-luc cells, likely as a result of their robust cell survival mechanisms [43]. In mouse tumors, the combination of DOX and oHA delivered by iRGD nanoparticles remarkably inhibited the recruitment of TAM into the tumor site more effectively than the free drug combination or iRGD-DOX-PLN treatments (Fig. 5 and Fig. S7). Given their phagocytic nature, TAMs are likely to take more nanoparticles compared to other immune cells, further enhancing the therapeutic impact of this approach [44].

IL-6, a cytokine produced by a wide variety of cell types, plays an essential role in mediating chronic inflammatory and cancer cell proliferation [45]. In the tumor microenvironment, IL-6 contributes to chemoresistance by preventing cancer cells from therapy-induced DNA damage, oxidative stress and apoptosis [46]. Our investigation on iRGD-DOX-oHA-PLN formulation at different DOX concentrations, could regulate IL-6 production in 4T1-luc and RAW 264.7 cells, performed using a co-culture setup depicted in Fig. 6E. The differentiation of murine RAW 264.7 macrophage cells towards a TAM-like phenotype driven by the secretion of monocyte colony-stimulating factor (M-CSF) [47] in Fig. 6F. Subsequent analysis of IL-6 levels in the supernatant from these co-cultured cells revealed that iRGD-DOX-oHA-PLN treatment led to a dose-dependent decrease in IL-6 production (Fig. 6G). Even at a low DOX concentration of 0.01 μg mL^{-1}, where cell viability is largely maintained (as indicated by MTT assays), the observed reduction in IL-6 suggests a disruption in relevant signaling pathways governing IL-6 production including MAPK/ERK, PI3K-Akt, and their downstream NF-κB [48]. We further investigated the impact of the different treatments on IL-6 production in 4T1-luc cells alone and found that IL-6 levels increased with only DOX-containing formulation, whereas formulations containing oHA led to a reduction in IL-6 levels (Fig. 6H). The suppression of IL-6 holds a significant potential not only to remodel the immunosuppressive TME but also to potentially enhance the sensitivity of cancer cells to chemotherapy.

3.9. *In vivo anti-tumor and anti-metastasis effect of iRGD-DOX-oHA-PLN*

The therapeutic potential of iRGD-DOX-oHA-PLN was compared against treatments with saline, free DOX, free DOX + oHA, and iRGD-DOX-PLN in inhibiting the primary tumor growth and suppressing lung metastasis in the orthotopic murine 4T1-luc tumors. Tumors were inoculated in the 4th mammary fat pad of female BALB/c mice 3 weeks prior treatment (Week-3). Treatments were given biweekly at week 0 and week 2, respectively, and mice were sacrificed at week 4. All groups received intravenous injections at an equivalent DOX dose of 10

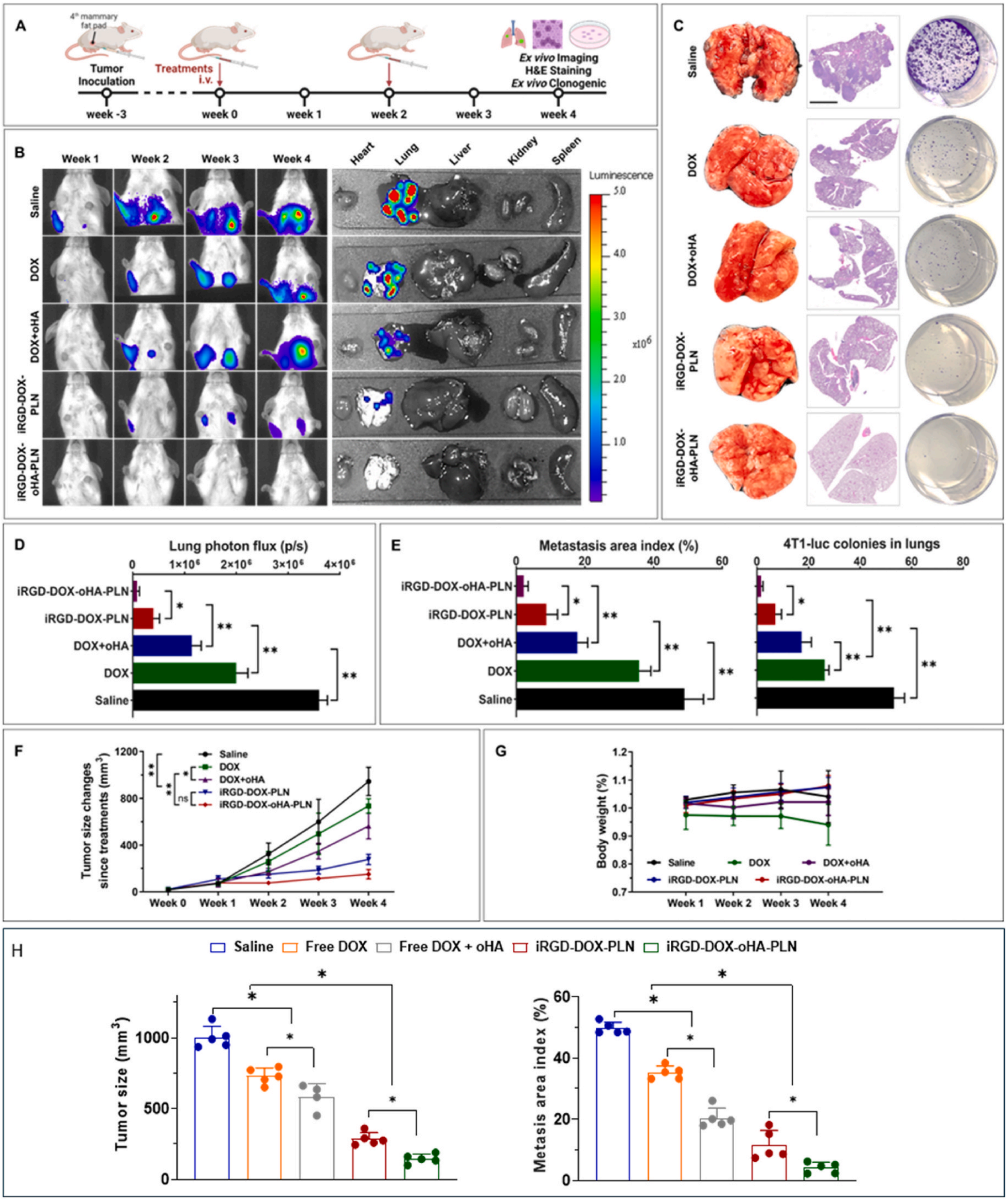

Fig. 7. The iRGD-DOX-oHA-PLN reduced lung metastasis and inhibited tumor growth in the metastatic TNBC mouse model. A) Timeline of tumor inoculation, treatment, animal sacrifice, and subsequent analyses. Female BALB/c mice were orthotopically inoculated with 4T1-luc tumor cells two weeks prior to treatment initiation (defined as week 0). Intravenous treatments with saline, free DOX, free DOX + oHA, iRGD-DOX-PLN, or iRGD-DOX-oHA-PLN (all at a DOX concentration of 10 mg kg^{-1}) were administered at week 0 and week 2 post-inoculation. At week 4, mice were sacrificed, and organs were collected for analysis. **B)** Left panel: representative *in vivo* bioluminescence images of lung metastases progression over the tumor growth period. Right panel: *ex vivo* bioluminescence images of major organs. **C)** Representative images of whole lungs, H&E-stained lung sections (scale bar = 2.5 mm), and *ex vivo* 4T1-luc colonies isolated from the lungs. **D)** Quantitative analysis of *ex vivo* lung bioluminescence (photon efflux). N = 5. **E)** Quantitative analysis of metastasis area index and *ex vivo* 4T1-luc colonies isolated from lungs. N = 5. **F)** Primary tumor size changes as a function of time. N = 5. **G)** Mouse body weight changes as a function of time. **H)** Comparisons of tumor volumes and metastasis area index in lungs at week 4. All data are presented as mean ± SD. $^{*}p < 0.05$. $^{**}p < 0.01$.

mg kg^{-1}. The experimental design, including the treatment schedule, the timing of animal sacrifice, and subsequent analyses, are outlined in Fig. 7A.

The development of lung metastases was monitored weekly using luciferin-induced bioluminescence imaging targeted to the lung region. At week 4, the animals were euthanized, and *ex vivo* bioluminescence imaging of major organs was performed. In the saline group, lung metastases became apparent as early as one week after treatment initiation, whereas a delay in metastatic signal emergence was observed in all other treatment groups (Fig. 7B). Notably, no detectable metastases were observed in the iRGD-DOX-oHA-PLN group. The chronological order of bioluminescence signal appearance and intensity, indicating the progression of lung metastases, was as follows: saline > free DOX > DOX + oHA > iRGD-DOX-PLN > iRGD-DOX-oHA-PLN, with the iRGD-DOX-oHA-PLN group exhibiting the weakest or absent lung signal, suggesting effective inhibition of metastatic spread. The bioluminescence signals of major organs were quantitated (Fig. 7D). The iRGD-DOX-oHA-PLN treated group displayed a significantly low bioluminescent signal compared with other groups. Moreover, the H&E staining of the lungs revealed healthy tissue histology in the iRGD-DOX-oHA-PLN group, in contrast to other treatment groups, further substantiating the metastasis-inhibiting effect of the iRGD-DOX-oHA-PLN (Fig. 7C).

In a subset of animals, the lungs were harvested at week 4 for single-cell suspension preparation. The cells were cultured in 4T1-luc cell culture media containing 6-thioguanine to select for the 6-thioguanine-resistant 4T1-luc cells only and inhibit the growth of other cell types over 6 days [49]. The iRGD-DOX-oHA-PLN treatment significantly reduced 4T1-luc colony formation compared to other treatments (Fig. 7C). Quantitative analyses of the metastasis area index and isolated 4T1-luc colonies in the lungs revealed the most robust reduction in lung metastases in iRGD-DOX-oHA-PLN treated animals (Fig. 7E).

The size of primary tumor at week 4 was the smallest in the mice treated with iRGD-DOX-oHA-PLN, with a notably 80 % smaller compared to the free DOX group (Fig. 7F) [50].

The enhanced therapeutic efficacy of iRGD-DOX-oHA-PLN can be attributed to multiple mechanisms. Firstly, the effective targeting of integrins by the iRGD-peptide enhanced drug delivery directly to the tumor (Fig. 2). Secondly, co-delivered oHA contributes to inhibition of key tumor growth signaling pathways, specifically RHAMM/p-ERK and CD44/PI3K [28]. Lastly, our formulation remodeled the immunosuppressive TME, thereby bolstering the favorable immune response against the tumor. These multifaceted mechanisms are comprehensively depicted and supported by the data in Figs. 3–5.

The safety profiles of these treatments were also assessed by monitoring the changes in body weight, appearance, and behavior and through histological analyses using H&E staining. Treatment-induced changes in body weight revealed a significant loss (~6 %) exclusively in the free DOX-treated animals. In contrast, mice in the other treatment groups maintained relatively stable weights (Fig. 7G). Notably, the mice treated with iRGD nanoparticles demonstrated a continual increase in body weight, suggesting a higher safety of this formulation. Representative images of H&E-stained major organs of mice sacrificed at week 4 post-treatments demonstrate the presence of metastases in harvested organs in the saline, free DOX and free DOX-oHA treatment groups (Fig. S8). DOX-associated toxicities were apparent in the groups treated with free DOX as mice presented ruffled fur and lethargic movement post-treatment. Other treatment groups showed no such signs of morbidity. Specifically, the formation of degenerative vacuoles in the cardiomyocytes was only spotted in the free DOX treatment group, indicating the presence of cardiotoxicity.

Compared to saline, free DOX inhibited tumor growth by approximately 27 %, while free DOX + oHA achieved ~42 % inhibition. The nanoparticle formulation further enhanced efficacy, with iRGD-DOX-PLN reaching ~72 % inhibition. Most notably, iRGD-DOX-oHA-PLN suppressed tumor growth by ~86 % versus saline, demonstrating the strongest antitumor activity among all groups (Fig. 7H).

The integration of oHA and iRGD peptide with doxorubicin presents a strategic approach to inhibit metastasis in TNBC by targeting the CD44-integrin signaling axis. CD44 plays a central role in promoting tumor cell adhesion, migration, and metastasis through its interaction with integrins, particularly β1 and α6β4, as demonstrated in basal-like breast cancer models [51,52]. Upon binding to its ligand, CD44 activates integrin signaling cascades involving focal adhesion proteins such as talin, paxillin, and cortactin, facilitating extravasation and colonization of distant organs. Incorporation of oHA in the drug delivery system enables selective targeting of CD44-overexpressing TNBC cells, disrupting their integrin-mediated adhesion and motility [51,53].

In addition to enhancing targeting, low-molecular-weight oHA disrupts CD44 and RHAMM clustering, attenuating PI3K/Akt and MAPK/ERK signaling pathways involved in chemoresistance, epithelial-mesenchymal transition (EMT), and DNA repair. This disruption reduces IL-6 secretion, potentially via suppression of the STAT3 feedback loop, and downregulates drug efflux transporters such as breast cancer resistance protein (BCRP) and P-glycoprotein (P-gp) [54,55]. These combined effects enhance intracellular DOX retention and cytotoxicity while promoting immune activation, further strengthening the anti-metastatic efficacy of the iRGD-DOX-oHA-PLN system in TNBC.

Meanwhile, the iRGD peptide enhances tumor penetration by interacting with αvβ3/β5 integrins and neuropilin-1, further potentiating the intratumoral accumulation of doxorubicin [26,27]. This dual-targeting strategy not only suppresses CD44–integrin-dependent metastatic signaling but also remodels the TME to inhibit pre-metastatic niche formation, as supported by evidence of CD44-integrin cooperation in organotropic metastasis and exosomal signaling [52]. Thus, leveraging oHA and iRGD synergistically with doxorubicin offers a rational and mechanistically supported anti-metastatic therapy for aggressive TNBC.

3.10. Analysis of patient survival in relation to immune markers

To further support the translational relevance of our findings, we utilized BC-GenExMiner (Breast Cancer Gene-Expression Miner), a web-based statistical tool that aggregates and analyzes gene expression and prognostic data from publicly available breast cancer datasets, including those from Gene Expression Omnibus (GEO), ArrayExpress, and the Cancer Genome Atlas Program (TCGA) [56,57]. These datasets are derived from ethically approved studies with informed patient consents. The gene expression profiles are generated through standardized DNA microarray analysis procedures, which involve RNA extraction from tumor samples, reverse transcription to cDNA, hybridization to oligonucleotide microarray chips (e.g., Affymetrix U133A or U133 Plus 2.0), followed by fluorescence-based signal detection and normalization using algorithms such as RMA or MAS5 [58]. This integrative approach enables correlations evaluation between immune markers and patient survival outcomes in TNBC, thereby linking our preclinical immunomodulatory findings to clinically meaningful prognostic indicators.

Our findings in the preclinical studies demonstrated that treatment with iRGD-DOX-oHA-PLN in the orthotopic 4T1 TNBC mouse model increased tumor infiltration of $CD4^+$ and $CD8^+$ T cells, along with the downregulation of TAMs and IL-6, compared to the saline control and other treatment groups. To illustrate the clinical relevance of these observations, we performed a bioinformatic analysis of TNBC patients' survival in relation to several immune markers in patients' samples. The analysis has revealed that high expression levels of CD4, CD8A, and CD8B, along with low expression of adhesion G protein-coupled receptor E1 (ADGRE1, also known as F4/80 antigen, expressed by TAMs [59]) and IL-6, are correlated with improved disease-free survival (DFS), in line with our preclinical results (Fig. 8). Furthermore, the significant anti-tumor and anti-metastatic effects observed in the syngeneic mouse tumor model suggest that the immune modulation may reflect similar mechanisms in human TNBC subjects. Specifically, enhancing T-cell activity (as indicated by CD4 and CD8 expression) and reducing pro-tumorigenic factors (such as ADGRE1 and IL-6) could contribute to

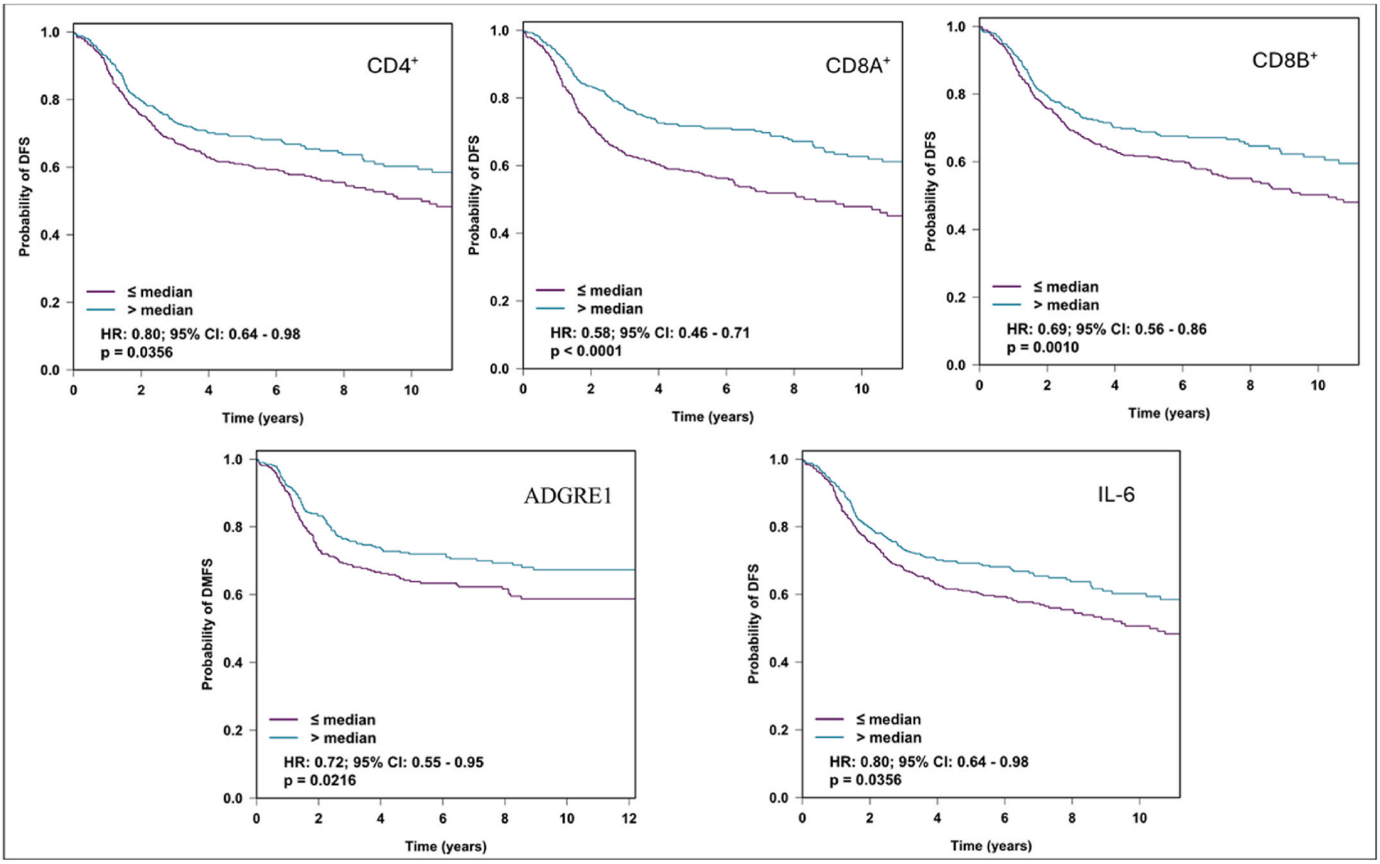

Fig. 8. Kaplan-Meier overall survival analyses of low and high CD4, CD8A, CD8B, ADGRE1, and IL-6 expression in the tumors of TNBC patients based on DNA microarray data. CD4 low: n = 436; CD4 high: n = 430; CD8A low: n = 434; CD8A high: n = 432; CD8B low: n = 457; CD8B high: n = 409; ADGRE1 low: n = 140; ADGRE1 high: n = 34; IL6 low: n = 469; IL6 high: n = 463.

better outcomes in future treatments.

4. Conclusion

We have developed a synergistic combination nanomedicine, iRGD-DOX-oHA-PLN for remodeling the tumor immune microenvironment and enhancing chemotherapy of metastatic TNBC treatment. The iRGD-peptide-conjugated nanoparticles delivered DOX and oHA successfully to the integrin overexpressing TNBC cells and tumors, where oHA synergizes with DOX to enhance the anticancer efficacy and induce ICD. The co-delivered DOX and oHA acted collectively to remodel the immunosuppressive TME, enhancing CD4$^+$ and CD8$^+$ T cell infiltration and activation, as evidenced by the increased granzyme B and IFN-γ, while reducing Immunosuppressive TAMs and Treg cells. Consequently, systemic administration of iRGD-DOX-oHA-PLN significantly inhibited growth of primary tumor and prevented metastasis in secondary organs, suggesting its therapeutic potential in the treatment of TBNC. While these findings demonstrate strong therapeutic potential, successful clinical translation of iRGD-DOX-oHA-PLN will require addressing several challenges, including scalable synthesis of nanoparticles, and thorough evaluation of systemic safety and immunogenicity.

CRediT authorship contribution statement

Ibrahim Alradwan: Writing – original draft, Methodology, Investigation, Formal analysis, Conceptualization. **Pei Zhi:** Writing – review & editing, Investigation, Data curation. **Abdulmottaleb E. Zetrini:** Validation, Resources, Conceptualization. **Liting Wang:** Writing – review & editing, Software, Formal analysis. **Chunsheng He:** Writing – review & editing, Supervision, Conceptualization. **Mahya Rezaeifarimani:** Methodology. **Jeffrey T. Henderson:** Writing – review & editing, Supervision, Conceptualization. **Andrew M. Rauth:** Writing – review & editing, Writing – original draft, Validation, Project administration, Data curation. **Xiao Yu Wu:** Writing – review & editing, Supervision, Resources, Project administration, Funding acquisition, Conceptualization.

Consent to participate

Consent to participate is not applicable for the data presented in Fig. 8 as the data were analyzed from a publicly available breast cancer dataset.

Ethics approval

All animal experiments were approved by local and governmental animal experimental committees and carried out according to national and institutional guidelines of UHN (University Health Network) (Animal Use Protocol 4333; animal welfare committee, University of Toronto, Canada).

Declaration of competing interest

The authors declare no competing interests.

Data Availability

All data generated or analyzed during this study are included in this published article and its supplementary information files.

Funding

This research was supported by grants from the Canadian Institutes of Health Research (CIHR), NSERC of Canada, scholarships from King Abdulaziz City for Science and Technology (KACST), Saudi Aradia, Ontario Graduate Scholarship (OGS), Canada, and the Chinese Scholarship Council.

Declaration of competing interest

The authors declare that they have no known competing financial interests or personal relationships that could have appeared to influence the work reported in this paper.

Acknowledgments

The authors thank the Canadian Institutes of Health Research (CIHR) for the project grant and the National Science and Engineering Research Council (NSERC) of Canada for the Equipment Grants and funding to X. Y.Wu. The Ontario Graduate Scholarship (OGS) and the Graduate Department of Pharmaceutical Sciences, University of Toronto, Canada for student support. The King Abdulaziz City for Science and Technology (KACST), Saudi Arabia for the scholarship to I. Alradwan. The Chinese Scholarship Council, China for the scholarship to P. Zhi. The technical contribution in the breast tumor sample processing and immunohistochemistry staining from Dr. Andrew J. Elia, Staff Scientist, Centre for Integrative Immune Analysis, CIIA Histology Core, Princess Margaret Cancer Centre, PMH/University Health Network. Ibrahim Alradwan and Pei Zhi equally contributed to this work.

Appendix A. Supplementary data

Supplementary data to this article can be found online at https://doi.org/10.1016/j.mtbio.2025.102445.

Supplemental Information

Additional experimental data includes the following. DOX to oHA ratios, and size and charge, and summary of physicochemical characteristics of NP (Figs. S1 and S2 respectively). Growth inhibition *in vitro* (Fig. S3). In vitro anti-migration and invasion, and wound healing (Figs. S4 and S5, respectively). NP biodistribution studies *in vivo* and *ex vivo* (Fig. S6). IHC staining for CD86 and CD206 (Fig. S7). *Ex vivo* H&E (Fig. S8).

Data availability

Data will be made available on request.

References

[1] L. Yin, J.-J. Duan, X.-W. Bian, S.-c. Yu, Triple-negative breast cancer molecular subtyping and treatment progress, Breast Cancer Res. 22 (2020) 61.

[2] J. Cortes, D.W. Cescon, H.S. Rugo, Z. Nowecki, S.A. Im, M.M. Yusof, C. Gallardo, O. Lipatov, C.H. Barrios, E. Holgado, H. Iwata, N. Masuda, M.T. Otero, E. Gokmen, S. Loi, Z.F. Guo, J. Zhao, G. Aktan, V. Karantza, P. Schmidi, Randomized, double-blind, phase III study of pembrolizumab plus chemotherapy versus placebo plus chemotherapy for previously untreated locally recurrent inoperable or metastatic triple-negative breast cancer, J. Clin. Oncol. 38 (2020).

[3] P. Schmid, J. Cortes, R. Dent, L. Pusztai, H. McArthur, S. Kummel, J. Bergh, C. Denkert, Y.H. Park, R. Hui, N. Harbeck, M. Takahashi, M. Untch, P.A. Fasching, F. Cardoso, J. Andersen, D. Patt, M. Danso, M. Ferreira, M.A. Mouret-Reynier, S. A. Im, J.H. Ahn, M. Gion, S. Baron-Hay, J.F. Boileau, Y. Ding, K. Tryfonidis, G. Aktan, V. Karantza, J. O'Shaughnessy, K.- Investigators, Event-free survival with pembrolizumab in early triple-negative breast cancer, N. Engl. J. Med. 386 (2022) 556–567.

[4] C. Corti, B. Koca, T. Rahman, E.A. Mittendorf, S.M. Tolaney, Recent advances in immune checkpoint inhibitors for triple-negative breast cancer, ImmunoTargets Ther. 14 (2025) 339–357.

[5] A. Gunjur, A.J. Manrique-Rincon, O. Klein, A. Behren, T.D. Lawley, S.J. Welsh, D. J. Adams, 'Know thyself' - host factors influencing cancer response to immune checkpoint inhibitors, J. Pathol. 257 (2022) 513–525.

[6] A. Labani-Motlagh, M. Ashja-Mahdavi, A. Loskog, The tumor microenvironment: a milieu hindering and obstructing antitumor immune responses, Front. Immunol. 11 (2020).

[7] K. Khalaf, D. Hana, J.T. Chou, C. Singh, A. Mackiewicz, M. Kaczmarek, Aspects of the tumor microenvironment involved in immune resistance and drug resistance, Front. Immunol. 12 (2021) 656364.

[8] P.M. Witschen, T.S. Chaffee, N.J. Brady, D.N. Huggins, T.P. Knutson, R.S. LaRue, S. A. Munro, L. Tiegs, J.B. McCarthy, A.C. Nelson, K.L. Schwertfeger, Tumor cell associated Hyaluronan-CD44 signaling promotes pro-tumor inflammation in breast cancer, Cancers (Basel) 12 (2020).

[9] C. Chen, S. Zhao, A. Karnad, J.W. Freeman, The biology and role of CD44 in cancer progression: therapeutic implications, J. Hematol. Oncol. 11 (2018) 64.

[10] S.L. Liu, C.H. Cheng, Akt signaling is sustained by a CD44 splice isoform-mediated positive feedback loop, Cancer Res. 77 (2017) 3791–3801.

[11] J.E. Rayahin, J.S. Buhrman, Y. Zhang, T.J. Koh, R.A. Gemeinhart, High and low molecular weight hyaluronic acid differentially influence macrophage activation, ACS Biomater. Sci. Eng. 1 (2015) 481–493.

[12] Y. Hong, Y.K. Kim, G.B. Kim, G.H. Nam, S.A. Kim, Y. Park, Y. Yang, I.S. Kim, Degradation of tumour stromal hyaluronan by small extracellular vesicle-PH20 stimulates CD103(+) dendritic cells and in combination with PD-L1 blockade boosts anti-tumour immunity, J. Extracell. Vesicles 8 (2019) 1670893.

[13] A. Almalik, H. Benabdelkamel, A. Masood, I.O. Alanazi, I. Alradwan, M. A. Majrashi, A.A. Alfadda, W.M. Alghamdi, H. Alrabiah, N. Tirelli, A.H. Alhasan, Hyaluronic acid coated chitosan nanoparticles reduced the immunogenicity of the formed protein Corona, Sci. Rep. 7 (2017) 10542.

[14] I. Alradwan, P. Zhi, T. Zhang, H. Lip, A. Zetrini, C. He, J.T. Henderson, A.M. Rauth, X.Y. Wu, Nanoparticulate drug combination inhibits DNA damage repair and PD-L1 expression in BRCA-mutant and wild type triple-negative breast cancer, J. Contr. Release 377 (2025) 661–674.

[15] M. Song, T. Liu, C. Shi, X. Zhang, X. Chen, Bioconjugated manganese dioxide nanoparticles enhance chemotherapy response by priming tumor-associated macrophages toward M1-like phenotype and attenuating tumor hypoxia, ACS Nano 10 (2016) 633–647.

[16] H.A. Wahba, H.A. El-Hadaad, Current approaches in treatment of triple-negative breast cancer, Cancer Biol Med 12 (2015) 106–116.

[17] A. Ahmed, S.W.G. Tait, Targeting immunogenic cell death in cancer, Mol. Oncol. 14 (2020) 2994–3006.

[18] O. Kepp, L. Senovilla, I. Vitale, E. Vacchelli, S. Adjemian, P. Agostinis, L. Apetoh, F. Aranda, V. Barnaba, N. Bloy, L. Bracci, K. Breckpot, D. Brough, A. Buqué, M. G. Castro, M. Cirone, M.I. Colombo, I. Cremer, S. Demaria, L. Dini, A.G. Eliopoulos, A. Faggioni, S.C. Formenti, J. Fučíková, L. Gabriele, U.S. Gaipl, J. Galon, A. Garg, F. Ghiringhelli, N.A. Giese, Z.S. Guo, A. Hemminki, M. Herrmann, J.W. Hodge, S. Holdenrieder, J. Honeychurch, H.-M. Hu, X. Huang, T.M. Illidge, K. Kono, M. Korbelik, D.V. Krysko, S. Loi, P.R. Lowenstein, E. Lugli, Y. Ma, F. Madeo, A. A. Manfredi, I. Martins, D. Mavilio, L. Menger, N. Merendino, M. Michaud, G. Mignot, K.L. Mossman, G. Multhoff, R. Oehler, F. Palombo, T. Panaretakis, J. Pol, E. Proietti, J.-E. Ricci, C. Riganti, P. Rovere-Querini, A. Rubartelli, A. Sistigu, M.J. Smyth, J. Sonnemann, R. Spisek, J. Stagg, A.Q. Sukkurwala, E. Tartour, A. Thorburn, S.H. Thorne, P. Vandenabeele, F. Velotti, S.T. Workenhe, H. Yang, W.-X. Zong, L. Zitvogel, G. Kroemer, L. Galluzzi, Consensus guidelines for the detection of immunogenic cell death, OncoImmunology 3 (2014) e955691.

[19] A. Takeuchi, T. Saito, CD4 CTL, a cytotoxic subset of CD4+ T cells, their differentiation and function, Front. Immunol. 8 (2017).

[20] M.A. Amini, A.Z. Abbasi, P. Cai, H. Lip, C.R. Gordijo, J. Li, B. Chen, L. Zhang, A. M. Rauth, X.Y. Wu, Combining Tumor microenvironment modulating nanoparticles with Doxorubicin to enhance chemotherapeutic efficacy and boost antitumor immunity, JNCI: J. Natl. Cancer Inst. 111 (2019) 399–408.

[21] A.E. Zetrini, H. Lip, A.Z. Abbasi, I. Alradwan, T. Ahmed, C. He, J.T. Henderson, A. M. Rauth, X.Y. Wu, Remodeling Tumor immune microenvironment by using polymer-lipid-manganese dioxide nanoparticles with radiation therapy to boost immune response of castration-resistant, Prostate Cancer 6 (2023) 247.

[22] H. Lip, A. Zetrini, E. Park, P. Cai, A.Z. Abbasi, T. Huyan, I. Alradwan, A.M. Rauth, X.Y. Wu, Mitigating radioresistance mechanisms by polymer-lipid manganese dioxide nanoparticles enhances immunogenic cell death and antitumor immune response to facilitate abscopal effect in breast tumor models, Drug Deliv. Transl. Res. (2025), https://doi.org/10.1007/s13346-025-01873-1. Epub ahead of print. PMID: 40389728.

[23] M. Yang, J. Zhou, L. Lu, D. Deng, J. Huang, Z. Tang, X. Shi, P.-C. Lo, J.F. Lovell, Y. Zheng, H. Jin, Tumor cell membrane-based vaccines: a potential boost for cancer immunotherapy, Exploration 4 (2024) 20230171.

[24] J. Li, Y. Wu, Y. Li, H. Zhu, Z. Zhang, Y. Li, Glutathione-Disrupting nanotherapeutics potentiate ferroptosis for treating luminal androgen receptor-positive triple-negative breast cancer, ACS Nano 18 (2024) 26585–26599.

[25] S. Zheng, M. Li, W. Xu, J. Zhang, G. Li, H. Xiao, X. Liu, J. Shi, F. Xia, C. Tian, K. I. Kamei, Dual-targeted nanoparticulate drug delivery systems for enhancing triple-negative breast cancer treatment, J. Contr. Release : official journal of the Controlled Release Society 371 (2024) 371–385.

[26] H. Zuo, iRGD: a promising peptide for cancer imaging and a potential therapeutic agent for various cancers, J. Oncol. 2019 (2019) 9367845.

[27] N. Stojanovic, A. Dekanic, M. Paradzik, D. Majhen, K. Ferencak, J. Ruscic, I. Bardak, C. Supina, M.T. Tomicic, M. Christmann, M. Osmak, A. Ambriovic-Ristov, Differential effects of Integrin alphav Knockdown and cilengitide on

sensitization of triple-negative breast cancer and melanoma cells to microtubule poisons, Mol. Pharmacol. 94 (2018) 1334–1351.

[28] T. Zhang, C. Fu, I. Alradwan, T. Yen, H. Lip, P. Cai, A.M. Rauth, L. Zhang, X.Y. Wu, Targeting signaling pathways of hyaluronic acid and integrin receptors by synergistic combination nanocomposites inhibits systemic metastases and primary triple negative breast cancer, Adv. Therapeut. 4 (2021) 2100022.

[29] T.C. Chou, Drug combination studies and their synergy quantification using the chou-talalay method, Cancer Res. 70 (2010) 440–446.

[30] P. Jézéquel, M. Campone, W. Gouraud, C. Guérin-Charbonnel, C. Leux, G. Ricolleau, L. Campion, bc-GenExMiner: an easy-to-use online platform for gene prognostic analyses in breast cancer, Breast Cancer Res. Treat. 131 (2012) 765–775.

[31] A. Shalviri, H.K. Chan, G. Raval, M.J. Abdekhodaie, Q. Liu, H. Heerklotz, X.Y. Wu, Design of pH-responsive nanoparticles of terpolymer of poly (methacrylic acid), polysorbate 80 and starch for delivery of doxorubicin, Colloids Surf. B Biointerfaces 101 (2013) 405–413.

[32] A. Shalviri, G. Raval, P. Prasad, C. Chan, Q. Liu, H. Heerklotz, A.M. Rauth, X.Y. Wu, pH-Dependent doxorubicin release from terpolymer of starch, polymethacrylic acid and polysorbate 80 nanoparticles for overcoming multi-drug resistance in human breast cancer cells, Eur. J. Pharm. Biopharm. 82 (3) (2012), 587-59.

[33] H. Y Fan, G. Raval, A. Shalviri, S. May, X.Y. Wu, H. Heerklotz, Coupled equilibria of a self-associating drug loaded into polymeric nanoparticles, Methods 76 (2015) 162–170.

[34] T. Zhang, P. Prasad, P. Cai, C. He, D. Shan, A.M. Rauth, X.Y. Wu, Dual-targeted hybrid nanoparticles of synergistic drugs for treating lung metastases of triple negative breast cancer in mice, Acta Pharmacol. Sin. 38 (2017) 835–847.

[35] F. Danhier, A. Le Breton, V. Préat, RGD-Based strategies to target Alpha(v) Beta(3) integrin in cancer therapy and diagnosis, Mol. Pharm. 9 (2012) 2961–2973.

[36] D. Shan, J. Li, P. Cai, P. Prasad, F. Liu, A.M. Rauth, X.Y. Wu, RGD-conjugated solid lipid nanoparticles inhibit adhesion and invasion of αvβ3 integrin-overexpressing breast cancer cells, Drug Delivery and Translational Research 5 (2015) 15–26.

[37] R. Zander, D. Schauder, G. Xin, C. Nguyen, X.P. Wu, A. Zajac, W.G. Cui, CD4+T cell help is required for the Formation of a cytolytic CD8+ T cell subset that protects against chronic infection and cancer, Immunity 51 (2019) 1028–+.

[38] C. Termeer, F. Benedix, J. Sleeman, C. Fieber, U. Voith, T. Ahrens, K. Miyake, M. Freudenberg, C. Galanos, J.C. Simon, Oligosaccharides of Hyaluronan activate dendritic cells via toll-like receptor 4, J. Exp. Med. 195 (2002) 99–111.

[39] R. Roychoudhuri, R.L. Eil, N.P. Restifo, The interplay of effector and regulatory T cells in cancer, Curr. Opin. Immunol. 33 (2015) 101–111.

[40] S. Sauer, L. Bruno, A. Hertweck, D. Finlay, M. Leleu, M. Spivakov, Z.A. Knight, B. S. Cobb, D. Cantrell, E. O'Connor, K.M. Shokat, A.G. Fisher, M. Merkenschlager, T cell receptor signaling controls Foxp3 expression via PI3K, Akt, and mTOR, Proc. Natl. Acad. Sci. U. S. A. 105 (2008) 7797–7802.

[41] B. Ruffell, L.M. Coussens, Macrophages and therapeutic resistance in cancer, Cancer Cell 27 (2015) 462–472.

[42] W. Kang, D. Svirskis, V. Sarojini, A.L. McGregor, J. Bevitt, Z. Wu, Cyclic-RGDyC functionalized liposomes for dual-targeting of tumor vasculature and cancer cells in glioblastoma: an in vitro boron neutron capture therapy study, Oncotarget 8 (2017) 36614–36627.

[43] Y. Chen, Y. Song, W. Du, L. Gong, H. Chang, Z. Zou, Tumor-associated macrophages: an accomplice in solid tumor progression, J. Biomed. Sci. 26 (2019) 78.

[44] T. Zhang, H. Lip, C. He, P. Cai, Z. Wang, J.T. Henderson, A.M. Rauth, X.Y. Wu, Multitargeted nanoparticles deliver synergistic drugs across the blood–brain barrier to brain metastases of triple negative breast cancer cells and tumor-associated macrophages, Adv. Healthcare Mater. 8 (2019) 1900543.

[45] J. Chen, Y.H. Wei, W.Q. Yang, Q.N. Huang, Y. Chen, K. Zeng, J.W. Chen, IL-6: the link between inflammation, immunity and breast cancer, Front. Oncol. 12 (2022).

[46] N. Kumari, B.S. Dwarakanath, A. Das, A.N. Bhatt, Role of interleukin-6 in cancer progression and therapeutic resistance, Tumour Biol 37 (2016) 11553–11572.

[47] S. Sousa, R. Brion, M. Lintunen, P. Kronqvist, J. Sandholm, J. Monkkonen, P. L. Kellokumpu-Lehtinen, S. Lauttia, O. Tynninen, H. Joensuu, D. Heymann, J. A. Maatta, Human breast cancer cells educate macrophages toward the M2 activation status, Breast Cancer Res. 17 (2015) 101.

[48] T.T.T. Phan, N.V. Truong, W.G. Wu, Y.C. Su, T.S. Hsu, L.Y. Lin, Tumor suppressor p53 mediates interleukin-6 expression to enable cancer cell evasion of genotoxic stress, Cell Death Discov. 9 (2023) 340.

[49] H.E. Daaboul, C. Dagher, R.I. Taleb, K. Bodman-Smith, W.N. Shebaby, M. El-Sibai, M.A. Mroueh, C.F. Daher, β-2-Himachalen-6-ol inhibits 4T1 cells-induced metastatic triple negative breast carcinoma in murine model, Chem. Biol. Interact. 309 (2019) 108703.

[50] H. Tsukihara, F. Nakagawa, K. Sakamoto, K. Ishida, N. Tanaka, H. Okabe, J. Uchida, K. Matsuo, T. Takechi, Efficacy of combination chemotherapy using a novel oral chemotherapeutic agent, TAS-102, together with bevacizumab, cetuximab, or panitumumab on human colorectal cancer xenografts, Oncol. Rep. 33 (2015) 2135–2142.

[51] S. McFarlane, C. McFarlane, N. Montgomery, A. Hill, D.J.J. Waugh, CD44-mediated activation of α5β1-integrin, cortactin and paxillin signaling underpins adhesion of basal-like breast cancer cells to endothelium and fibronectin-enriched matrices, Oncotarget 6 (2015).

[52] W. Mu, Y. Xu, P. Gu, W. Wang, J. Li, Y. Ge, H. Wang, Exosomal CD44 cooperates with Integrin α6β4 to support organotropic metastasis via regulating tumor cell motility and target host cell activation, Engineering 7 (2021) 1413–1423.

[53] Z. Hao, M. Zhang, Y. Du, J. Liu, G. Zeng, H. Li, X. Peng, Invadopodia in cancer metastasis: dynamics, regulation, and targeted therapies, J. Transl. Med. 23 (2025) 548.

[54] H. Yuan, C. Qiu, X. Wang, P. Wang, L. Yi, X. Peng, X. Xu, W. Huang, Y. Bai, J. Wei, J. Ma, Y.K. Wong, C. Fu, W. Xiao, C. Chen, Y. Long, Z. Li, J. Wang, Engineering semiconducting polymeric nanoagonists potentiate cGAS-STING pathway activation and elicit long term memory against recurrence in breast cancer, Adv. Mater. 37 (2025) 2406662.

[55] L. Tang, M. Xie, J. Li, Y. Mei, Y. Cao, Q. Xiao, H. Dong, Y. Zhang, W. Wang, Leveraging nano-engineered mesenchymal stem cells for intramedullary spinal cord tumor treatment, Chin. Chem. Lett. 34 (2023) 107801.

[56] bc-GenExMiner/Breast Cancer Gene-Expression Miner, 2025.

[57] P. Jézéquel, W. Gouraud, F. Ben Azzouz, C. Guérin-Charbonnel, P.P. Juin, H. Lasla, M. Campone, bc-GenExMiner 4.5: New Mining Module Computes Breast Cancer Differential Gene Expression Analyses, Database : the Journal of Biological Databases and Curation, 2021, p. 2021.

[58] P. Jézéquel, H. Lasla, W. Gouraud, A. Basseville, B. Michel, J.S. Frenel, P.P. Juin, F. Ben Azzouz, M. Campone, Mesenchymal-like immune-altered is the fourth robust triple-negative breast cancer molecular subtype, Breast Cancer 31 (2024) 825–840.

[59] M. Laviron, M. Petit, E. Weber-Delacroix, A.J. Combes, A.R. Arkal, S. Barthélémy, T. Courau, D.A. Hume, C. Combadière, M.F. Krummel, A. Boissonnas, Tumor-associated macrophage heterogeneity is driven by tissue territories in breast cancer, Cell Rep. 39 (2022) 110865.